# Low-Order Modeling of Freely Vibrating Flexible Cables

by

Michael P. Davis

A Thesis

Submitted to the Faculty

of the

WORCESTER POLYTECHNIC INSTITUTE

In partial fulfillment of the requirements for the

Degree of Master of Science

in

Mechanical Engineering

by

---

May 2001

APPROVED:

---

Professor David Olinger, Major Thesis Advisor

---

Professor Michael Demetriou, Major Thesis Co-advisor

---

Professor James Hermanson, Committee Member

---

Professor Nikolaos Gatsonis, Graduate Committee Rep.

**Abstract**

A low-order, dynamical systems approach is applied to the modeling of flow induced vibrations of flexible cables. By combining a coupled map lattice wake model with a linear wave equation cable model, both the free response of the cable as well as the resulting wake structures are examined. This represents an extension of earlier coupled map lattice models that only modeled the wake of forced cable vibration. The validity of the model is assessed through comparisons with both Computational Fluid Dynamics models (NEKTAR spectral element code) and wake experiments.

The experimental wake data was collected through the use of hot-film anemometry techniques. Eight hot-film probes were placed along the span of a flexible cable mounted in the test section of a water tunnel. Through the use of frequency domain correlation algorithms, the phase of vortex shedding was calculated along the cable span from the hot-film velocity data.

Results for an elastically mounted rigid cylinder showed that the freely vibrating CML model predicted behavior characteristic of a self-induced oscillator; the maximum amplitude of vibration was found to occur at a cylinder natural frequency that did not coincide identically with the natural shedding frequency of the cylinder. Furthermore, the variation of the frequency of cylinder vibration with its natural frequency was seen to be linear.

For standing wave cable responses, the freely vibrating CML model predicted lace-like wake structures. This result is qualitatively consistent with both the NEKTAR simulations and experimental results. Little difference was found between the wakes of forced and freely vibrating cables at the Reynolds number of the study

$Re = 100$. Finally, it was found that the freely vibrating CML could match numerical predictions of cross-flow amplitude as the cable mass-damping parameter was varied over an order of magnitude (once the CML was tuned to match results at a specific mass-damping level).

In addition to providing wake patterns for comparisons with the freely vibrating CML, experimental data was supplied to a self-learning CML scheme. This self-learning CML was able to estimate the experimental wake data with good accuracy. The self-learning CML is seen as the next extension of the freely-vibrating CML model, capable of estimating unmodeled wake dynamics through the use of experimental data.

**Acknowledgements**

Foremost, I would like to acknowledge the assistance and guidance of my advisors, Professors David J. Olinger and Michael A. Demetriou, without whose insight this thesis would not have been possible. Additionally, I would like to thank my remaining committee members, Professor James Hermanson and Professor Nikolaos Gatsonis for generously agreeing to fit me in to their busy schedules.

Special thanks go to Dr. George Karniadakis of Brown University, for providing the NEKTAR results upon which this thesis heavily depends.

I would like to acknowledge the Office of Naval Research for supporting this research.

Finally, I would like to thank the ME Secretaries for all their help in completing my degree requirements here at WPI.

# Contents

# List of Figures

# List of Tables

# Chapter 1

# Introduction

The interaction between fluid and elastic structural systems is an exciting and complex problem. Examples of fluid-structure interaction include the flutter of airplane wings, vibrational instabilities of turbine blades in gas turbine engines, and the wind induced vibrations of power lines, bridges, and other structures. Nearly all of these problems are characterized by a fluid instability at or near a resonant frequency of the structure being excited.

In the specific case of fluid flow over long, slender, cylindrical cables, the forcing from the fluid comes from the regular shedding of vortices in the cable wake. If the dominant wake frequencies happen to coincide with one of the natural frequencies of the cable, a resonance condition exists and large scale motions can ensue. This phenomenon is one of the primary reasons for failure in numerous marine cable applications; cables for towing, mooring buoys, and other similar arrangements have all been known to experience this self-excitation.

While the wake of low Reynolds number stationary rigid cylinders is well known and has been modeled successfully for many years, the wake of a flexible cable has not been as well studied. Even at Reynolds numbers as low as one hundred

three-dimensional complex wakes exist. Wake structures that have been observed in these cases include lace-like patterns, vortex-dislocations, and frequency cells. This complexity in the wake makes the system difficult to model. Efficient modeling that could serve as the basis for flow control algorithms are particularly difficult to develop.

Traditional methods of examining the system focus on either experimental programs or computational fluid dynamics (CFD) simulations. Newman and Karniadakis [14], [15] conducted studies of flow over a flexible cable at low Reynolds number using the spectral element CFD code (NEKTAR). The NEKTAR package was developed at Brown University by Professor George Karniadakis. These simulations will be used for comparisons to the present study.

In recent years, a new approach for the study of low Reynolds number wake flows has evolved. Aspects of the two dimensional cylinder wake have been successfully modeled [17] using tools borrowed from the field of nonlinear dynamics. These models have the advantage of being computationally efficient. These early studies have been extended to modeling the more complex problem of the wake behind a flexible cable that is *forced* externally at a particular frequency, amplitude, and mode shape [18].

The main goal of this thesis is to extend these low-order models to the case of self-excited, *freely* vibrating cables. Other goals include extensive comparisons of the dynamical systems approach to both NEKTAR simulations and experimental data. In addition, the results of this thesis will be integrated with a self-learning wake model that represents an additional level of complexity in the dynamical systems approach to modeling wake flows.

## 1.1 Wake of a Circular Cylinder at Low Reynolds Number

The two-dimensional wake of a circular cylinder at low Reynolds number ($Re < 150$) has a significant bearing on the more complex wakes of flexible cables. A brief description of the 2-D cylinder wake is therefore appropriate. An extensive review article on the vortex shedding process can be found in Bearman [1].

At Reynolds numbers below 55, (specific values will vary slightly from experiment to experiment) the wake behind a rigid circular cylinder is ordered and steady. A low pressure region exists on the back side of the cylinder because of the separation of the boundary layer in the presence of an adverse pressure gradient. As the Reynolds number increases from the Stokes flow regime, the separation location moves forward from the rear stagnation point to encompass nearly the entire back half of the cylinder.

Above $Re = 55$, a small instability develops in the two shear layers on opposite sides of the cylinder. At sufficiently high Reynolds number (roughly $Re = 65$) these shear layers will roll up in to the familiar Karman vortex street [25], characterized by the regular, periodic, staggered shedding of vortices in to the wake. The shedding frequency $f_{so}$ combined with the free stream velocity $U_\infty$ and cylinder diameter $d$ form a non-dimensional group known as the Strouhal number,

$$St = \frac{f_{so} d}{U_\infty}. \tag{1.1}$$

.

This two dimensional shedding frequency and the non-dimensional Strouhal number are vital parameters in the description of the three dimensional cable wake.

Empirical relations between the Strouhal number and the Reynolds number have

been determined [20],

$$St = \left(0.212 - \frac{4.5}{Re}\right). \tag{1.2}$$

For $Re = 100$, the Roshko relation gives $St = 0.167$.

The vortex street will remain laminar and roughly two dimensional up until around $Re = 100$. Above $Re = 90$, Tritton [24] noted the start of spanwise variations in wake structure along a rigid cylinder. Between $Re = 150$ and $Re = 300$, the wake transitions from being laminar to turbulent, and three dimensional effects become increasingly important. These effects have a strong dependence on the cylinder end conditions, and could include parallel or oblique shedding of vortices, spanwise frequency cells, and other phenomena [26].

## 1.2 Vortex Induced Vibrations and Lock-On

The behavior of the 2-D cylinder wake is invaluable in the study of vortex induced vibrations because the source of these vibrations is the Karman vortex street described previously. The alternate shedding of vortices creates a fluctuating lift force on the cylinder which results in cylinder motion. The oscillating lift force has the greatest effect on cylinder motion when the shedding frequency is in the neighborhood of the structural natural frequency of the cylinder.

Numerous experimental investigations have studied this problem. Koopman [10] studied an elastically mounted rigid cylinder, forced externally at a specific frequency, and discovered that the shedding frequency of the wake changed to match the cylinder's frequency under certain conditions. This effect, known as vortex lock-on, occurred whenever the natural shedding frequency of the cylinder - that is, the frequency at which the wake sheds when it is stationary and rigidly mounted - was

$\pm 25 - 30$ percent of the forcing frequency of the cylinder. This shifting of the shedding frequency, in apparent violation of the Strouhal relation, is a pivotal discovery in the study of vortex induced vibrations.

Two fundamental types of experiments in the study of vortex lock-on exist: those in which the cylinder is *externally forced* at a particular frequency, and experiments where the cylinder is allowed to *freely vibrate* in response to the wake. The relationship between the two different scenarios is not well understood. Is the wake behind an *externally forced* cylinder the same as the wake behind a *freely vibrating* cylinder at the same amplitude level with an identical natural frequency? In both cases lock on conditions can exist, with the shedding frequency of the cylinder adjusting to match the frequency of motion. This thesis seeks, in part, to address that question.

## 1.3 Non Linear Dynamics Applied to Wake Flows

Ever since Lorenz [11] pioneered the field of chaos and nonlinear dynamics with a reduced order model of the atmosphere, researchers have been attempting to model extremely complex systems with low dimensional nonlinear models. The concept of universality - that there might be some fundamental dynamical structure that applies to a wide range of systems - is at the core of this approach. By utilizing simple iterated maps qualitative results about the very essence of a system's dynamics are extracted.

For forced cylinder wakes, the appropriate basic dynamic structure is that of a coupled oscillator. An example of such a system from mechanics is a forced pendulum. Universal to all systems that are described as coupled oscillators is the lock-on effect set forth in the previous section.

Several different approaches have been used to attempt to model wake flows in

this way. The Landau-Stuart equation [19], Ginzburg-Landau equations [13], and van der Pol oscillators [22] have all been used to model the dynamics of wakes as coupled nonlinear oscillators.

Olinger [16] demonstrated that the forced wake of a 2-D elastically mounted cylinder can be modeled by the sine circle map,

$$\theta_{n+1} = \theta_n + \Omega - \frac{K}{2\pi}\sin(2\pi\theta_n). \tag{1.3}$$

This is the basic wake model that is used in this work, and will be developed in more detail later on. The main advantages of this approach are its simplicity and its computational efficiency.

By modeling the wake at a particular spanwise location of a flexible cable with a circle map oscillator, a finite number of oscillators can be coupled together in order to model the three dimensional cable wake. The output of the circle map is related to spanwise vorticity; hence, its diffusion is the coupling mechanism between oscillators. Olinger [17] developed a model for the *forced* wake of flexible cables, termed the Coupled Map Lattice (or CML), in this manner. This CML is the starting point for the work presented here.

## 1.4 Thesis Objectives

The primary goal of this thesis is the extension of the *forced* cable wake model proposed in the CML to include *freely* vibrating cables. This was accomplished by adding to the CML the structural dynamics of the cable. In the forced wake models, the cable mode shape, amplitude level, and forcing frequency were all inputs to the system. There was no need to include the dynamic response of the cable. In order to study lock on conditions and wake patterns of cables that self excite and are free

to vibrate on their own in response to the wake, the addition of the cable dynamics is necessary.

Through comparisons with NEKTAR simulations of freely vibrating flexible cables [14] the feasibility of this approach was determined. In doing so, methods of comparing the two sets of results will needed to be developed due to the differences in the type of data each methodology produces. The successful corroboration of the dynamical systems approach has broad implications for the use of these methods in control algorithms and other situations where computational efficiency is required.

In addition, experimental results were acquired for comparison. The wake behind a flexible cable placed in a water tunnel was measured using hot-film anemometry techniques. A rake system using eight hot-film probes placed at different locations along the cable span was used to collect velocity time histories. The velocity traces in the wake show elements of periodicity, arising from the regular shedding of vortices in the wake. By examining phase differences between the probes, the distribution of the phase lag of the shedding process can be calculated along the cable span. Correlation routines to perform these calculations were developed. The output of the correlation algorithm is the shedding pattern of the wake.

Finally, it is important to consider the context in which this study occurred. The CML as a tool to model complex wakes is not a stand alone approach. Free input parameters exist within the model. Setting these precise input values requires empirical data. In addition, the simplistic nature of the models suggest that there will always exist underlying wake dynamics that are going unmodeled. In an attempt to overcome this, this thesis is but a piece of a larger study designed to use the CML as the core of a self-learning control problem. The actual dynamics are assumed to be a combination of the CML output and an unmodeled portion; the self-learning algorithm attempts to deduce the unknown dynamics from supplied wake data.

Initially, this wake data is taken from the CFD studies mentioned above. The eventual goal of the overall effort is that the self-learning CML would be able to utilize laboratory wake data in real time in order to successfully account for the unmodeled wake dynamics. This thesis seeks to both extend the scenarios that coupled map lattices can model to include freely vibrating cables, as well as to provide some of the initial wake data from experiments for use in the self-learning algorithm.

# Chapter 2

# Low-Order Modeling of Flexible Cable Wakes

## 2.1 Nonlinear Dynamics in Cylinder Wakes

In order to develop the coupled map lattice (CML), first consider a rigid cylinder with diameter $d$ placed in a uniform freestream $U_\infty$. The shedding frequency $f_{so}$ of the stationary cylinder can be obtained from its Strouhal number $St$, given in Equation 1.1. The cylinder is forced by some external means in the crossflow direction with an amplitude $K$ at the frequency $f_e$. The shedding and forcing frequencies form an unforced frequency ratio $\Omega$ defined as

$$\Omega = \frac{f_{so}}{f_e}. \tag{2.1}$$

Olinger [16] has shown that low order iterative models from the study of nonlinear dynamics of coupled oscillators may be successful in modeling the forced cylinder wake. A common map used in the investigation of two coupled non-linear oscillators is the sine circle map, presented below:

$$\theta_{n+1} = \theta_n + \Omega - \frac{K}{2\pi}\sin(2\pi\theta_n). \tag{2.2}$$

Abstractly, the phase space of this system describes a torus. If a section of the torus is taken (termed a Poincare section), the angle at which state trajectories intersect this cross-section on the $nth$ revolution around the torus is the angle $\theta_n$. This situation is presented in Figure 2.1, showing a state trajectory and its intersection with a Poincare plane.

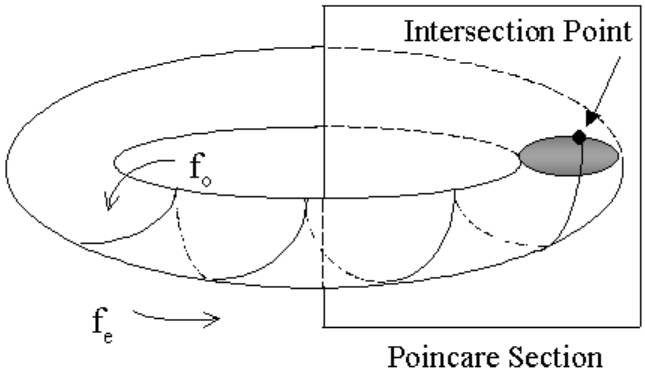


Figure 2.1: Schematic of Phase Space for Sine Circle Map

The angle $\theta_n$ represents the phase of the vortex shedding process. When $\theta_n = 0$, the vortex is just initiating the shedding process at the cylinder. When $\theta_n = 1$, the vortex has completed its shedding cycle (with the next cycle just beginning).

If the sequence of iterates $\theta_n$ continually intersects with an integer number of specific points on the Poincare section, than a lock-on condition results. Conversely, quasi-periodic conditions will result in the filling in of the Poincare section. The two parameters $\Omega$ and $K$ completely describe the system and determine whether a

lock-on or quasi-periodic state exists. Figure 2.2 shows two different scenarios, one in which a 3/1 lock on state exists, and the second showing a quasiperiodic system.

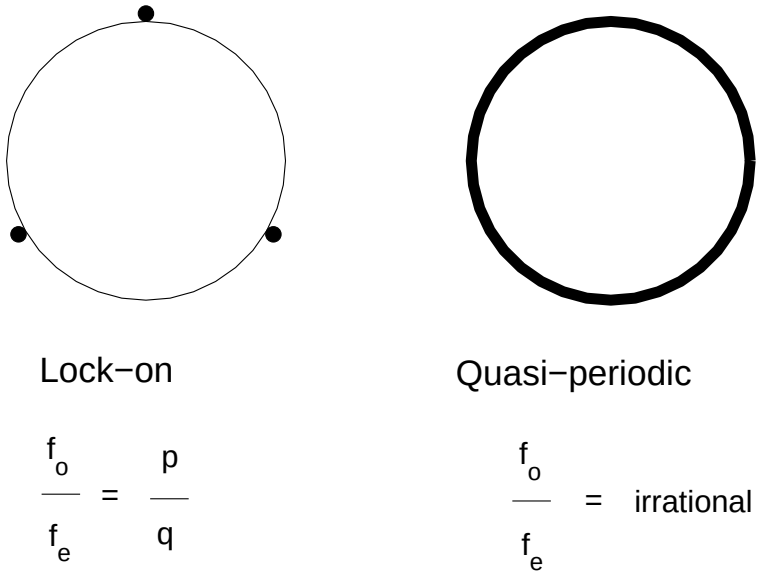


Figure 2.2: Poincare Sections for Lock-On (left) and Quasiperiodic (right) Conditions

The long-term $\theta$ behavior of the Sine Circle Map can be used to determine the lock-on state (if it exists). If $\theta_0$ is the initial state of the system, then the forced frequency ratio $\omega$, where

$$\omega = \lim_{n\to\infty} \frac{(\theta_n - \theta_0)}{n}, \tag{2.3}$$

provides a means for studying the system's dynamics. Rational values of the ratio $\omega$ indicate lock-on states, where as irrational values are the result of quasi-periodicity. Where the unforced shedding frequency ($f_{so}$) of the cylinder was determined from the

Strouhal relation, $\omega$ provides the shedding frequency of the oscillating cylinder, $f_s$. This is done by realizing that the definition of $\omega$ through Equation 2.3 is equivalent to stating

$$\omega = \frac{f_s}{f_e}. \tag{2.4}$$

The complete behavior of the Circle Map (Eq. 2.2) is best set forth in the $K$ vs. $\Omega$ diagram [9], presented in Figure 2.3. Several definitive "tongues" can be seen and are labeled with the appropriate fractional lock-on state. Regions of the $K$ - $\Omega$ plane not labeled are quasi-periodic states.

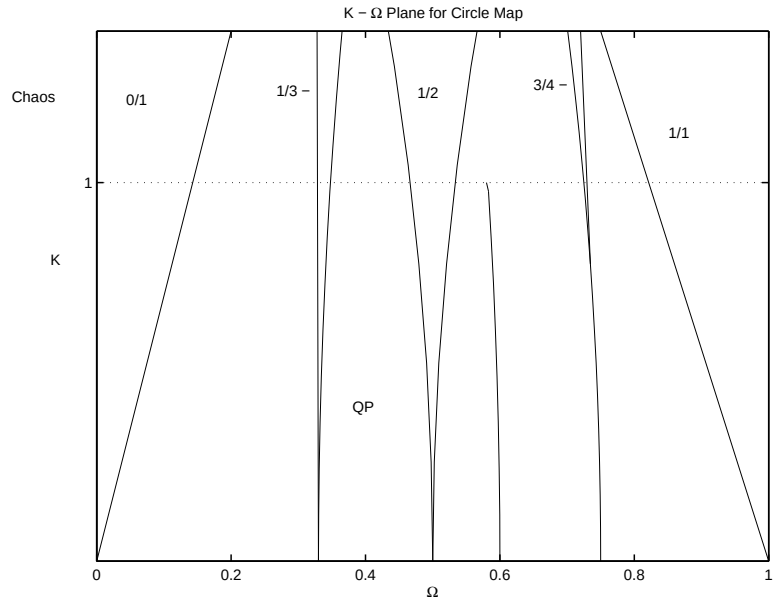


Figure 2.3: K - Ω Plane for the Sine Circle Map

### 2.1.1 The Coupled Map Lattice

In order to extend the utility of low-order maps such as the sine circle map to a third dimension, and hence *flexible* cables, a new system is needed. To accomplish this

extension, Olinger [18] proposed a coupled map lattice (CML). A series of $k^*$ circle map oscillators are placed along the span of the cable. These oscillators are then coupled through a diffusion model. The relevant equation is the diffusive vorticity transport equation,

$$\frac{\partial \omega}{\partial t} = -u \cdot \nabla \omega + \omega \cdot \nabla u + \nu \nabla^2 \omega, \tag{2.5}$$

where $\omega$ is the vorticity vector and $u$ is the velocity vector. This equation is simplified by making several assumptions. The streamwise and transverse vorticity components are dropped, spanwise vorticity is assumed to only depend on the spanwise direction, spanwise velocity variations are neglected, and the spanwise velocity component is assumed to be zero. Applying these assumptions to Equation 2.5 gives

$$\frac{\partial \omega_z}{\partial t} = \nu \frac{\partial^2 \omega_z}{\partial z^2}. \tag{2.6}$$

In related studies [3] additional terms in Equation 2.5 have been retained. In future work, these terms might also be included in a freely vibrating CML model.

In this model, $\omega_z$ denotes the vorticity in the spanwise ($z$) direction, and $\nu$ is the kinematic viscosity of the fluid. Employing an explicit finite difference algorithm to Equation 2.6, and establishing a correspondence between the spanwise vorticity $\omega_z$ as $\theta_n^k$ (where $k$ denotes discrete spanwise location, $n$ time iteration),

$$\theta_{n+1}^k = (1 - 2\epsilon)\theta_n^k + \epsilon(\theta_n^{k+1} + \theta_n^{k-1}). \tag{2.7}$$

The term $\epsilon$ is a stability parameter for the finite difference algorithm, and is found from

$$\epsilon = \frac{\nu \Delta t}{(\Delta z)^2}. \tag{2.8}$$

In order to couple Equation 2.7 to the Circle Map of Equation 2.2, the creation of an intermediate variable is required. The resulting system of equations for the diffusively coupled CML become

$$\theta_{n+1}^k = (1-2\epsilon)F_n^k + \epsilon(F_n^{k+1} + F_n^{k-1}), \tag{2.9}$$

$$F_n^k = \theta_n^k + \Omega - \frac{K^k}{2\pi}\sin\left[2\pi\theta_n^k - \phi_1^k - \frac{\pi}{2}\right] \tag{2.10}$$

Equation 2.9 is the finite difference form of the diffusion model described above, and Equation 2.10 is the sine circle map with some modifications. The phase angle $\phi_1^k$ represents the phase between a vortex being shed and the resulting cylinder motion. Values for $\phi_1^k$ have been determined by Olinger [18] from two-dimensional numerical simulations. These same values are used in the present study. A schematic of the coupled map lattice can be seen in Figure 2.4.

The coordinate system has the $x$, $y$, and $z$ directions corresponding to the streamise, transverse, and spanwise directions, respectively. Since there is now a spanwise coordinate, both $\theta$ and $K$ from the original circle map (Equation 2.2) now include a $k$ superscript. There are $k^*$ circle map oscillators (represented by the circles in Figure 2.4) placed along the cable span. Recall that $\theta_n^k = 0$ represents incipient vortex formation, while $\theta_n^k = 1$ is the complete shedding of the vortex. The characteristic non-dimensional spacing between vortices ($x^*$) can be calculated from the non-dimensional vortex convection velocity ($U_c/U_\infty$) and non-dimensional frequency ($St$):

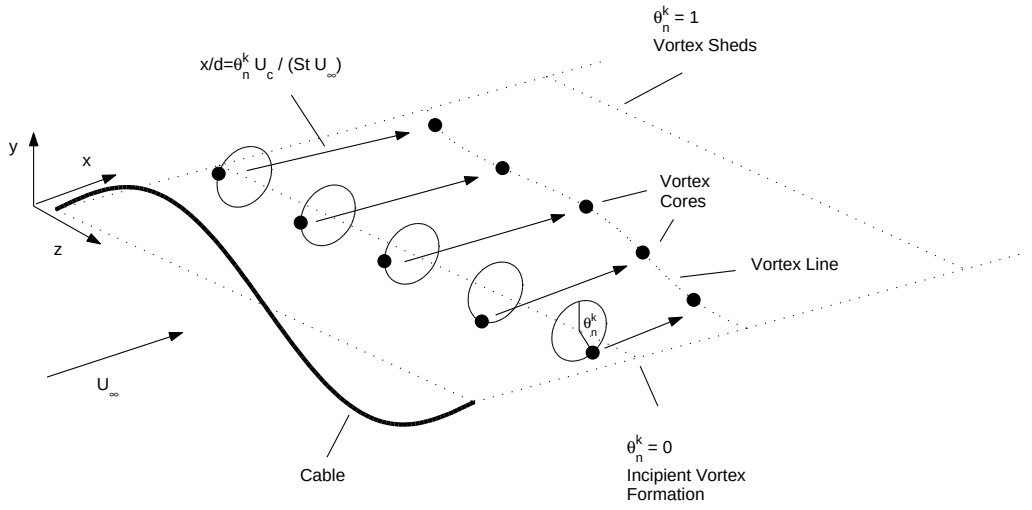


Figure 2.4: Schematic Diagram of Coupled Map Lattice

$$x^* = \frac{1}{St}\frac{U_c}{U_\infty}. \tag{2.11}$$

Using $x^*$, the value of $\theta_n^k$ at each spanwise location can be transformed into a downstream vortex location,

$$\frac{x}{d}_n^k = \theta_n^k x^* = \frac{\theta_n^k U_c}{StU_\infty}. \tag{2.12}$$

Through this transformation, the $\theta_n^k$ output of the CML is converted into a vortex shedding pattern.

In the 2-D model, $K$ represented the amplitude of forcing. If it was desired to model rigid cylinders, $K^k$ would be a constant. In order to model both standing and traveling wave mode shapes in *flexible* cables, $K^k$ will now very along the span according to

$$K^k = K_0 \cos\left[\frac{2\pi(k - nk_t)}{k_{wave}}\right]. \tag{2.13}$$

The new parameters $k_t$ and $k_{wave}$ specify either a traveling wave or a standing wave forcing.

The coupled map lattice wake model described in this section are the results of earlier work at WPI [18]. The inputs to the map are the frequency and amplitude of external forcing, number of lattice sites, free-stream Reynolds number, vortex convection velocity, Strouhal number, and various phase angles. It is important to emphasize at this point that the coupled map lattice model is not a stand alone approach. Several of the inputs to the map (i.e., vortex convection velocity [26], Strouhal number relation [20], and certain relevant phase angles [18]) are obtained from previous experimental and numerical studies on the wakes of circular cylinders. A fundamental understanding of the dynamics of the wake of a circular cylinder is necessary in order to successfully employ the CML approach.

In the next sections, the extension of the coupled map lattice to the modeling of freely vibrating cables will be discussed. This new model, which will henceforth be referred to as the freely vibrating CML model, no longer requires the frequency and amplitude of vibration of the cable as input parameters. Rather, through the use of a wave-equation model for the structural dynamics of the cable, the frequency and amplitude of vibration will be determined by the model. This freely vibrating CML model will require new inputs into the map in the form of free gain parameters that will be necessary to couple the CML wake model with the structural model. Once again, this approach will be heavily dependent on reference data from previous wake studies. Typical vibration amplitudes for freely vibrating cables are obtained through NEKTAR spectral element simulations and their values are used to tune the free parameters in the map.

## 2.2 Second Order Wave Equation

The stated main goal of this thesis is the extension of the current level of CML development to a model capable of representing self-excited cable responses. The cable mode shape that is set in Equation 2.13 for modeling externally forced cables is this replaced with a dynamic structural model of the cable. The free response of the cable can then be studied by coupling this cable model to a wake model that closely resembles the CML described in the previous section.

Consider a flexible cable with negligible bending stiffness placed in a uniform free stream. A schematic of this problem is presented in Figure 2.5.

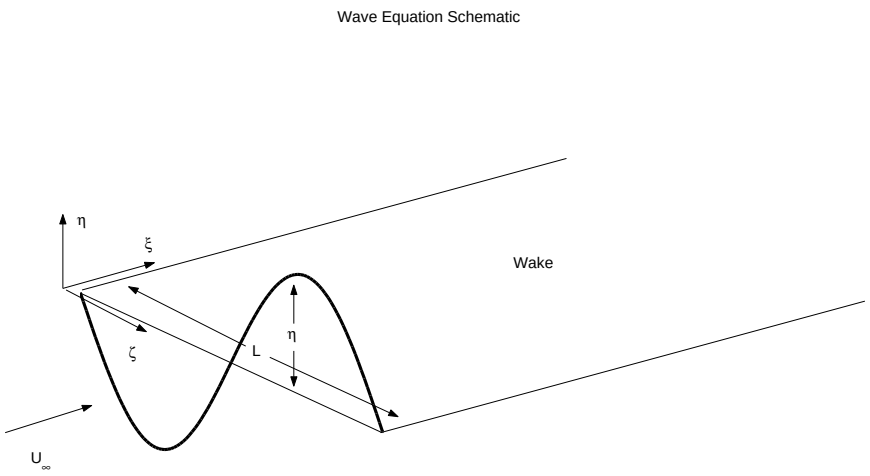


Figure 2.5: Schematic of Vibrating Cable Problem

The three coordinate directions $\xi$, $\eta$, and $\zeta$ represent the streamwise, crossflow, and spanwise directions, respectively. The cable has mass per unit length $\sigma$, tension $\tau$, and length $L$. The partial differential equation governing its motion in the crossflow direction is the linear wave equation [6],

$$\sigma \frac{\partial^2 \eta}{\partial t^2} = \tau \frac{\partial^2 \eta}{\partial \zeta^2} + f(\zeta, t), \tag{2.14}$$

subject to the initial conditions

$$\eta(\zeta, 0) = h(\zeta), \tag{2.15}$$

$$\frac{\partial \eta}{\partial t}(\zeta, 0) = g(\zeta), \tag{2.16}$$

and fixed boundary conditions,

$$\eta(0, t) = 0, \tag{2.17}$$

$$\eta(L, t) = 0. \tag{2.18}$$

The function $f(\zeta, t)$ is the lift force imparted by the fluid on the cable in the $\eta$ direction. In practice, vibrations in the streamwise direction will also occur due to an oscillating drag force. However, the crossflow direction has been observed to be the primary direction of cable motion, and therefore in this study the cable will be constrained to move only in the $\eta$, $\zeta$ plane.

Equation 2.14 can be re-written in terms of a wave speed by dividing through by $\sigma$

$$\frac{\partial^2 \eta}{\partial t^2} = c^2 \frac{\partial^2 \eta}{\partial \zeta^2} + \frac{f(\zeta, t)}{\sigma}. \tag{2.19}$$

The wave speed, $c$ is found from

$$c = \sqrt{\frac{\tau}{\sigma}}. \tag{2.20}$$

### 2.2.1 Non-Dimensional Form of the Wave Equation

For analysis, it is desired to get Equation 2.19 in a non-dimensional form. If all length variables are non-dimensionalized by the cable diameter, $d$, Equation 2.19 can be recast in terms of the new variables $z$, $y$, where

$$z = \frac{\zeta}{d}, \tag{2.21}$$

$$y = \frac{\eta}{d}. \tag{2.22}$$

After making the substitutions, the resulting PDE becomes

$$d\frac{\partial^2 y}{\partial t^2} = \frac{c^2}{d}\frac{\partial^2 y}{\partial z^2} + \frac{f(\zeta,t)}{\sigma}. \tag{2.23}$$

Define a time scale, $t^*$, in terms of the free-stream velocity $U_\infty$ and diameter $d$ as

$$t^* = \frac{tU_\infty}{d}, \tag{2.24}$$

and substitute into Equation 2.23, divide through by $U_\infty$, and multiply through by $d$, giving

$$\frac{\partial^2 y}{\partial t^{*2}} = \frac{c^2}{U_\infty^2}\frac{\partial^2 y}{\partial z^2} + \frac{df(\zeta,t)}{U_\infty^2\sigma}. \tag{2.25}$$

The $\frac{c^2}{U_\infty^2}$ term can be replaced by a non-dimensional wave speed, $c^{*2}$.

Define a mass ratio to be the cylinder mass divided by the mass of the displaced fluid (per unit length)

$$\rho = \frac{\sigma}{\frac{\pi}{4}d^2\rho_F}. \tag{2.26}$$

Here, $\rho_F$ is the fluid density. Solving for the cylinder mass, the forcing term (call it $F_y$) can be written as

$$F_y = \frac{df(\zeta,t)}{U_\infty^2 \rho \frac{\pi}{4} d^2 \rho_F}. \tag{2.27}$$

The $f(\zeta,t)$ term can be thought of as a lift per unit length and cast in terms of a lift coefficient, $C_l$

$$f(\zeta,t) = C_l \frac{1}{2} \rho_F U_\infty^2 d. \tag{2.28}$$

This lift coefficient will be the forcing term from the cable wake. It is useful here to consider it a function of the non-dimensional variables $z$ and $t^*$.

$$C_l = f(z,t^*) \tag{2.29}$$

Substituting these results into Equation 2.27.

$$F_y = \frac{C_l}{\rho \frac{\pi}{2}} \tag{2.30}$$

Thus, the final non-dimensional PDE becomes

$$\frac{\partial^2 y}{\partial t^{*2}} = c^{*2} \frac{\partial^2 y}{\partial z^2} + \frac{2C_l}{\pi \rho}. \tag{2.31}$$

The initial and boundary conditions become

$$y(z,0) = h(z), \tag{2.32}$$

$$\frac{\partial y}{\partial t^*}(z,0) = g(z), \tag{2.33}$$

$$y(0,t^*) = 0, \tag{2.34}$$

$$y(AR, t^*) \;=\; 0. \tag{2.35}$$

The variable $AR$ in the final boundary condition is the aspect ratio of the cable $L/d$.

In all discussions to follow throughout this thesis, it is assumed that all variables presented will be non-dimensional. Thus the $\xi$, $\eta$, and $\zeta$ coordinate directions are transformed to the $x$, $y$, and $z$ directions, respectively. In addition, the $*$ superscripts will be dropped from the non-dimensional time and wave speeds for clarity.

### 2.2.2 Finite Difference Representation

It is now desired to examine a finite difference solution to the homogeneous problem (Equation 2.31 with zero forcing term). Using a centered-time, centered-space finite difference operator, Equation 2.19 becomes

$$\frac{Y^k_{n+1} - 2Y^k_n + Y^k_{n-1}}{\Delta t^2} = c^2 \frac{(Y^{k+1} - 2Y^k + Y^{k-1})_{n+\theta}}{\Delta z^2}, \tag{2.36}$$

where the $n$ subscript denotes time (iteration) level, and the $k$ superscript is the nodal $z$ location.

#### Midpoint Leapfrog Method

A fully explicit scheme results when $\theta$ is set to zero in Equation 2.36. Solving Equation 2.36 for $Y^k_{n+1}$

$$Y^k_{n+1} = 2Y^k_n - Y^k_{n-1} + c^2 \frac{\Delta t^2}{\Delta z^2}(Y^{k-1} - 2Y^k + Y^{k+1})_n. \tag{2.37}$$

Equation 2.37 depends on both $Y_n$ and $Y_{n-1}$, and therefore requires knowledge of two previous iteration levels. Thus, two sets of initial data are needed.

A solution at time level 0 is provided by the first initial condition (Equation

2.15). Time level 1 can be obtained by considering a finite difference approximation to the second initial condition (Equation 2.16).

$$\frac{Y_1^k - Y_0^k}{\Delta t} = g(z^k), \tag{2.38}$$

$$Y_1^k = \Delta t\, g(x) + Y_0^k. \tag{2.39}$$

In the case that $g(z) = 0$,

$$Y_1^k = Y_0^k, \tag{2.40}$$

and Equation 2.37 becomes

$$Y_1^k = Y_0^k + \frac{c^2 \Delta t^2}{2\Delta z^2}(Y^{k-1} - 2Y^k + Y^{k+1})_0. \tag{2.41}$$

**Stability Analysis of Leapfrog Method**

Before proceeding to solving Equation 2.37 for a given set of initial and boundary conditions, it is necessary to examine the stability of the finite difference algorithm. This will be important in determining appropriate values of the time step $\Delta t$ to ensure stable solutions. The stability analysis that is applied is the method of Von Neumann [8]. While references most likely exist that present the stability analysis of the mid-point leapfrog finite difference algorithm applied to a linear wave equation, the major results were derived and are presented below with out reference.

Define an error term as the difference between the analytic and numeric solutions of Equation 2.14 as

$$\epsilon_n^k = y(z^k, n\Delta t) - Y_n^k. \tag{2.42}$$

It can be demonstrated that $\epsilon$ is also a solution to Equation 2.14. Writing the leapfrog finite difference representation in terms of the error yields

$$\epsilon_{n+1}^k = 2\epsilon_n^k - \epsilon_{n-1}^k + D^2(\epsilon^{k+1} - 2\epsilon^k + \epsilon^{k+1})_n, \tag{2.43}$$

where

$$D^2 = \frac{c^2\Delta t^2}{\Delta z^2}. \tag{2.44}$$

In the method of Von Neumann [8], replace $\epsilon_n^k$ by its Fourier expansion,

$$\epsilon_n^k = A_n \exp(j\sigma z). \tag{2.45}$$

The error at locations $k \pm 1$ are found to be

$$\begin{aligned} \epsilon_n^{k\pm1} &= A_n \exp(j\sigma(z \pm \Delta z)), & (2.46)\\ &= A_n \exp(j\sigma z)\exp(\pm j\sigma\Delta z), & (2.47)\\ &= \exp(\pm j\sigma\Delta z)\epsilon_n^k. & (2.48) \end{aligned}$$

In addition, the error at the $n+1$ time level is

$$\epsilon_{n+1}^k = A_{n+1} \exp(j\sigma z). \tag{2.49}$$

Substituting the above in to Equation 2.43 yields

$$\epsilon_{n+1}^k = 2\epsilon_n^k - \epsilon_{n-1}^k + D^2\epsilon_n^k(\exp(-j\sigma\Delta z) - 2 + \exp(j\sigma\Delta z)). \tag{2.50}$$

Dividing through by $\epsilon_n^k$ and utilizing Euler's equation gives

$$\gamma = 2 - \gamma^{-1} - 2D^2(1 - \cos(\sigma\Delta z)), \tag{2.51}$$

where

$$\gamma = \frac{\epsilon_{n+1}^k}{\epsilon_n^k}. \tag{2.52}$$

The variable $\gamma$ represents the propagation of error from one time level to the next. In order for a given finite difference representation to be stable, the magnitude of $\gamma$ must be less than unity. Rearranging 2.51,

$$\gamma^2 + 2[D^2(1 - \cos(\sigma\Delta z)) - 1]\gamma + 1 = 0. \tag{2.53}$$

Equation 2.53 is quadratic in $\gamma$. It can be shown that in order for the roots of Equation 2.53 to be stable, the following must hold:

$$\frac{c}{a} \leq 1, \tag{2.54}$$

$$|b| \leq a + c, \tag{2.55}$$

with

$$a = 1, \tag{2.56}$$

$$b = 2[D^2(1 - \cos(\sigma\Delta z)) - 1], \tag{2.57}$$

$$c = 1. \tag{2.58}$$

The first of the two stability conditions is obviously satisfied. The second requires

that

$$-2 \leq 2[D^2(1-\cos(\sigma\Delta z))-1] \leq 2 \tag{2.59}$$

The $(1-\cos(\sigma\Delta z))$ term has maximum and minimum values of 2 and 0, respectively. The 0 case is uninteresting (yielding $-2 \leq -2 \leq 2$) and of little use. The case when $(1-\cos(\sigma\Delta z)) = 2$ gives

$$\begin{aligned} -2 &\leq 2(2D^2-1) \leq 2, & (2.60)\\ 0 &\leq 4D^2 \leq 4, & (2.61)\\ 0 &\leq D^2 \leq 1, & (2.62)\\ 0 &\leq D \leq 1. & (2.63) \end{aligned}$$

Thus, in order for the solution of Equation 2.37 to be stable,

$$\frac{c\Delta t}{\Delta z} \leq 1. \tag{2.64}$$

**Model Validation - Test Cases**

Before moving on to the coupling of the wave equation to the Coupled Map Lattice, it is important to assess the validity and accuracy of the finite difference solution method proposed. In order to do this, consider the homogeneous version of Equation 2.19,

$$\frac{\partial^2 y}{\partial t^2} - c^2\frac{\partial^2 y}{\partial z^2} = 0. \tag{2.65}$$

The initial and boundary conditions are chosen such that they will coincide with the

initial and boundary conditions that will be utilized later on. In the CML studies to follow, a standing wave scenario with pinned end condition will be investigated. Thus, the appropriate initial conditions become

$$y(z,0) = \sin\left(\frac{2\pi z}{L}\right), \tag{2.66}$$

$$\frac{\partial y}{\partial t}(z,0) = 0. \tag{2.67}$$

This gives a second mode sinusoid as the initial cable displacement with zero initial velocity. The pinned boundary conditions are represented as

$$y(0,t) = 0, \tag{2.68}$$

$$y(L,t) = 0. \tag{2.69}$$

For simplicity, $L = 1$ is chosen for this example. Using 101 nodal $z$ locations and a time step of $\Delta t = 0.01$, the wave speed $c = 1$ is used in order to satisfy the stability condition from Equation 2.64. The finite difference solution to this test case as set out in Equation 2.37 is presented in Figure 2.6.

Figure 2.6 shows the standing wave output of the finite difference algorithm at several different time values. The initial displacement condition from Equation 2.66 is seen in the shape of the cable at time $t = 0$. A regular standing wave pattern exists (as is expected) with a vibration frequency equal to one cycle per second.

The accuracy of the solution can be evaluated by comparing the finite difference solution with an analytical one. Using a traveling wave interpretation, it can be shown [6] that the solution to Equation 2.65 with a zero initial condition on velocity

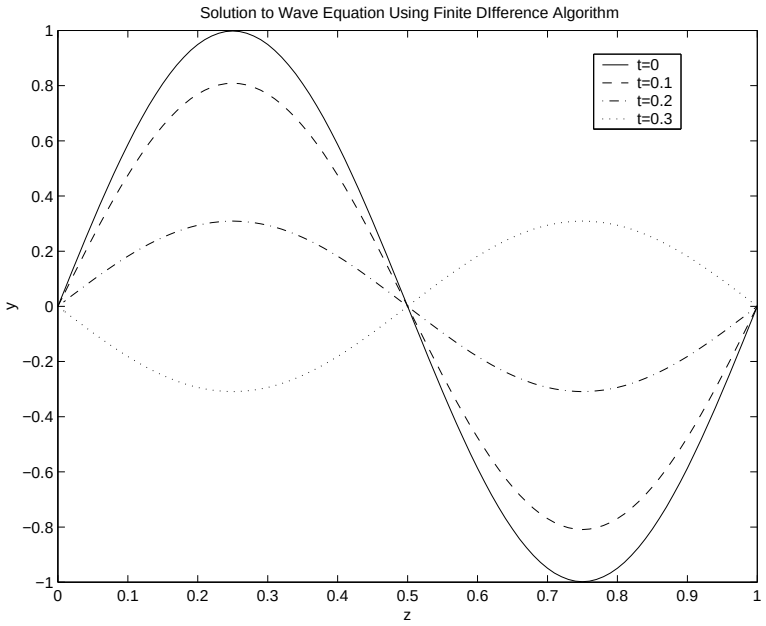


Figure 2.6: Standing Wave Finite Difference Solution to Wave Equation

is

$$y(z,t) = \frac{1}{2}[f_{ext}(z-ct) + f_{ext}(z-ct)], \tag{2.70}$$

where the function $f_{ext}(z)$ is the initial cable displacement, but defined in such as way so that it is $2L$ periodic and antisymmetric about $z = 0$ and $z = L$. In other words, if $f(z)$ is the initial cable displacement defined over the interval $0 < z < L$, then the half range sine expansion of $f(z)$ is identical to the Fourier series expansion of $f_{ext}(z)$. The second mode sine initial condition used above satisfies these periodicity and anti-symmetry requirements already, and therefore

$$f(z) = \sin\left(\frac{2\pi z}{L}\right) = f_{ext}(z). \tag{2.71}$$

The solution is given as

$$y(z,t) = \frac{1}{2}\left[\sin\left(\frac{2\pi(z-ct)}{L}\right) + \sin\left(\frac{2\pi(z+ct)}{L}\right)\right] \tag{2.72}$$

For the purposes of comparing the two outputs, Figure 2.7 plots the cable displacement at the first anti-node ($z = 0.25$) versus time for both the analytical solution (Equation 2.72) and the finite difference solution calculated and presented above.

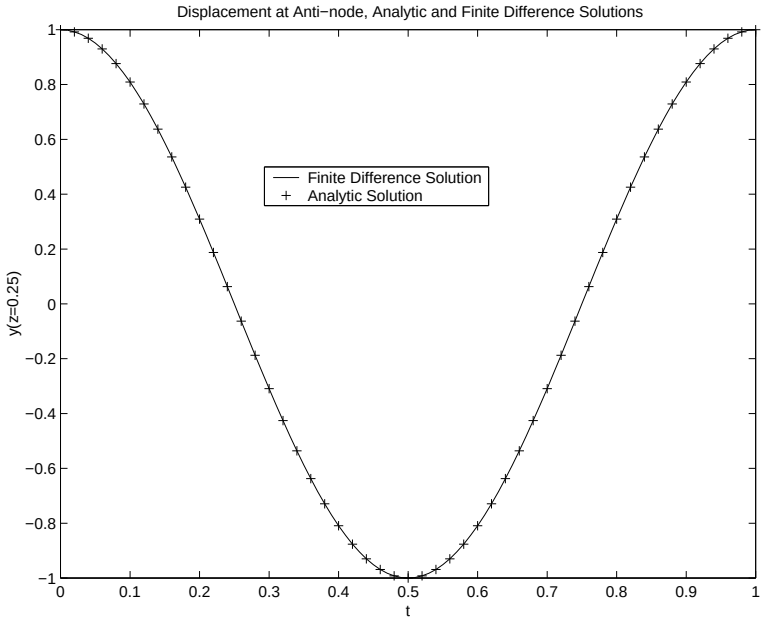


Figure 2.7: Comparison of Anti-node Displacement for Analytical, Numerical Solutions

## 2.3 Coupling of Wave Equation with CML

Prior to the present work the current state of development of the Coupled Map Lattice (CML) was restricted to the modeling of *externally* forced cables. The diffusively coupled CML is repeated below for convenience.

$$\theta_{n+1}^k = (1-2\epsilon)F_n^k + \epsilon(F_n^{k+1} + F_n^{k-1}), \tag{2.73}$$

$$F_n^k = \theta_n^k + \Omega - \frac{K_n^k}{2\pi}\sin\left[2\pi\theta_n^k - \phi_1^k - \frac{\pi}{2}\right], \tag{2.74}$$

The cable vibration frequency and mode shape are input to the CML through the frequency ratio $\Omega$ and cable amplitude $K^k$. In this model, the forcing term $K^k$ takes the form

$$K^k = K_0 \cos\left[\frac{2\pi(k-nk_t)}{k_{wave}}\right]. \tag{2.75}$$

Thus, both standing and traveling wave cables can be addressed.

A natural extension of the model would be to consider *freely* vibrating cables. In order to accomplish this the dynamics of the cable need to be included and coupled in to the CML. In order to compare the two different wake models, consider Figure 2.8.

The figure presents flow charts for both the forced and freely vibrating CML models. In the forced CML, the cable frequency and mode shape are input through the parameters $\Omega$ and $K_0$. The system is then iterated and the output of the map is the distribution of $\theta_n^k$ along the cable span. The freely vibrating CML flow chart has an additional box, representing the dynamics of the cable. The amplitude of vibration is no longer an input to the system. The natural frequency of the cable is

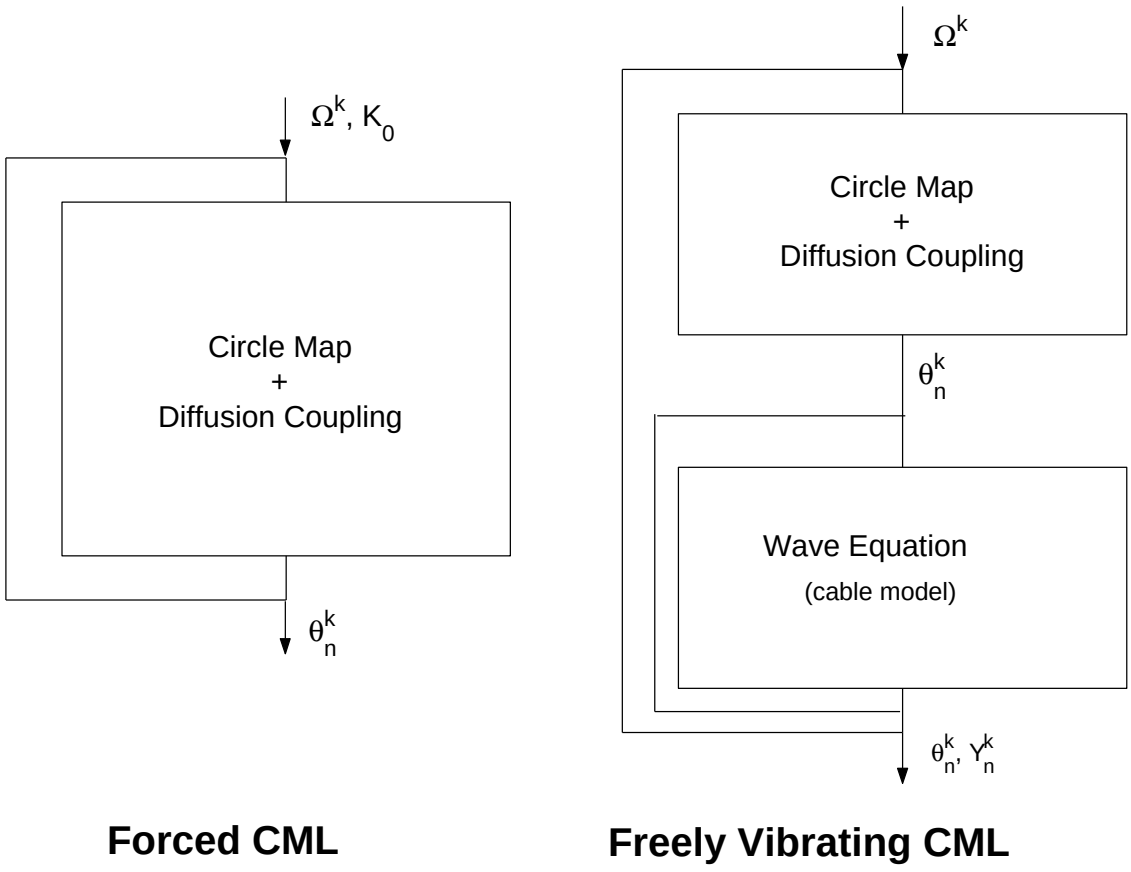


Figure 2.8: Schematic Comparing Forced and Freely Vibrating CML Models

specified in the $\Omega$ input term. After calculating the phase of vortex shedding, the wake model passes this information along to the cable model. For reasons that will become clear in later sections, the cable model then sub-iterates over a set number of time steps, and outputs the cable motion, $Y_n^k$, in addition to the wake parameter $\theta_n^k$.

### 2.3.1 2-D Model - Rigid Oscillating Cylinder

Before considering a model for a freely vibrating cable, the 2-D case (freely oscillating rigid cylinder) will be addressed. The wake of a rigid oscillating cylinder can be examined through the use of the sine-circle map, repeated below

$$\theta_{n+1} = \theta_n + \Omega - \frac{K}{2\pi}\sin(2\pi\theta_n). \tag{2.76}$$

In the forced vibration case, $\Omega$ represented the frequency ratio of the natural shedding frequency of the unforced cylinder ($\omega_{so}$) to the forcing frequency ($\omega_e$). Since it is now desired to examine free vibration, the forcing frequency in the denominator is replaced by the structural natural frequency of the cylinder,

$$\Omega = \frac{\omega_{so}}{\omega_n}. \tag{2.77}$$

The $K$ term in Equation 2.76 represented an amplitude level of forcing for the forced cylinder model. Again, in order to handle free vibration, this term needs to be related to the actual cylinder displacement (non-dimensionalized by cylinder diameter, $d$), $y$. This is accomplished by replacing $K$ in the original map by the displacement $y$ multiplied by a pre-determined gain factor $G$. This gain will be found by attempting to match maximum cylinder displacements in other studies (Newman and Karniadakis, 1996). The modified circle map for free vibration becomes

$$\theta_{(n+1)_1} = \theta_{n_1} + \Omega - \frac{Gy}{2\pi} \sin\left[2\pi\theta_{n_1} - \phi_1 - \frac{\pi}{2}\right]. \tag{2.78}$$

The 1 subscript on $\theta$ denotes the first of two shear layers. The phase angle $\phi_1$ represents the phase difference between the vortex shedding event and the corresponding cylinder motion, and is the same as the $\phi_1$ seen earlier in the forced CML expressions. In order to fully model the complete interaction between the cylinder and the wake, both shear layers need to be included. Thus, a second circle map oscillator modeling the second shear layer is included. This map is identical to the first with the exception of a phase shift of $\pi$ in the phase angle $\phi_1$ in order to account for the fact that the second shear layer will be 180 degrees out of phase with the first:

$$\theta_{(n+1)_2} = \theta_{n_2} + \Omega - \frac{Gy}{2\pi} \sin\left[2\pi\theta_{n_2} - (\phi_1 + \pi) - \frac{\pi}{2}\right]. \tag{2.79}$$

The dynamics of the rigid cylinder can be modeled as a second order linear spring mass damper system,

$$\rho\frac{d^2y}{dt^2} + b\frac{dy}{dt} + ky = f(t), \tag{2.80}$$

where $\rho$, $b$, and $k$, are the mass per unit length, damping, and stiffness of the cylinder. Written in terms of a damping ration $\zeta$ and natural frequency $\omega_n$, Equation 2.80 becomes

$$\frac{d^2y}{dt^2} + 2\zeta\omega_n\frac{dy}{dt} + \omega_n^2 y = \frac{f(t)}{\rho}. \tag{2.81}$$

All variables in this equation are non-dimensional; length and velocity scales are the cylinder diameter and free stream velocity, respectively, and the mass $\rho$ is non-dimensionalized by the mass of fluid the cylinder displaces.

The forcing term $f(t)$ is the lift force on the cylinder resulting from pressure and viscous forces imparted by the fluid. In order to couple the spring-mass-damper dynamics to the circle map model for the wake, the forcing term must somehow be related to the phase of vortex shedding, $\theta$. One potential method of doing this is to assume there is a sine dependence of lift-force on phase of shedding, with its amplitude set by a lift coefficient,

$$f(t) = \frac{2C_l}{\pi\rho} \sin(2\pi\theta_n - \phi_2). \tag{2.82}$$

The $2C_l/(pi\rho)$ term is a result of the dimensional arguments of Section 2.2.1. The lift coefficient, $C_l$, is a free parameter that will be set such that resulting cylinder amplitudes match other studies (much like the $G$ term from Equation 2.78). A second phase angle, $\phi_2$, is introduced to account for the phase lag of the lift force corresponding to a particular shedding cycle.

However, this only represents the forcing caused by a single shear layer. In order to model the resulting motion from both shear layers, the phase of the vortex shedding from the second shear layer needs to be included,

$$f(t) = \frac{2C_l}{\pi\rho} \left[\sin(2\pi\theta_{n_1} - \phi_2) - \sin(2\pi\theta_{n_2} - \phi_2)\right] \tag{2.83}$$

The second shear layer carries a minus sign since its net force will be in the opposite direction from the first shear layer. In the circle map expressions, it was mentioned that the phase angle $\phi_1$ for the second shear layer is $\pi$ out of phase with the first. Since the $\theta$ inputs to the forcing term already incorporates this alternate shedding behavior from the circle map, the phase angle $\phi_2$ includes no such shift and is the same for both shear layers.

The final step in the coupling of the wake and structural dynamics is the appro-

priate tuning of the cylinder's natural frequency. Using Equation 2.77 and recalling that the cylinder shedding frequency is related to the Strouhal number by

$$\omega_{so} = 2\pi St, \tag{2.84}$$

the natural frequency can be written in terms of $\Omega$ and $St$

$$\omega_n = \frac{2\pi St}{\Omega}. \tag{2.85}$$

### 2.3.2 3-D Model - Vibrating Cable

Much of the results developed in the previous section for a freely vibrating rigid cylinder can be extended in order to model a flexible cable. For this case, the wake model becomes the diffusively coupled CML (Equations 2.73 and 2.74) rather than the simple circle map. The cable model will be the linear wave equation presented earlier.

As in the externally forced cable, the cable dynamics will be input through the frequency ratio and $K^k$ forcing term. However, rather than pre-determining these parameters, they are output from a second order, one-dimensional wave equation used to account for the cable dynamics,

$$\frac{\partial^2 y}{\partial t^2} = c^2 \frac{\partial^2 y}{\partial z^2} + \frac{f(z,t)}{\rho}, \tag{2.86}$$

where $f(z,t)$ is the forcing from the wake vortex shedding, and $\rho$ is the cable mass ratio (cable mass to displaced water mass). Applying the midpoint leapfrog finite difference algorithm of Section 2.2.2 to Equation 2.86,

$$Y^k_{n+1} = 2Y^k_n - Y^k_{n-1} + c^2 \frac{\Delta t^2}{\Delta z^2}(Y^{k-1} - 2Y^k + Y^{k+1})_n + f^k_n. \tag{2.87}$$

The forcing term $f_n^k$ is related to the phase of vortex shedding ($\theta$) output from the CML, as in Section 2.3.1, through

$$f_n^k = \frac{2C_l}{\pi\rho}\left[\sin(2\pi\theta_{n_1}^k - \phi_2^k) - \sin(2\pi\theta_{n_2}^k - \phi_2^k)\right]. \tag{2.88}$$

As in the 2-D case, the amplitude factor $C_l$ is a free parameter and will be chosen so as to match other simulations. The phase angle $\phi_2$ represents the lag between a shedding event and its corresponding lift force.

As was seen in the 2-D model, the frequency ratio $\Omega$ takes on a slightly different meaning then it had in the externally forced CML. The natural frequencies of the cable, $\omega_n$, now take the place of the external excitation frequency, $\omega_e$. It can be shown that for the linear wave equation model with pinned ends, the natural frequencies of the cable will satisfy

$$\omega_n = \frac{n\pi c}{L}, \tag{2.89}$$

where $n$ indicates a particular mode. It is desired to examine lock on cases; that is, values of $\Omega$ at or near one. It is important to mention that in reporting $\Omega$, it is necessary to indicate which particular mode of the cable the Strouhal frequency is being tuned to. For example, an examination of the first mode cable response at $\Omega = 1$ would involve varying the cable tension such that the *first* natural frequency matched the cable shedding frequency. Similarly, a second mode study at $\Omega = 1$ would tune the cable tension to match its *second* natural frequency with the shedding frequency, and so on.

It has been shown that the wake dynamics appear in the wave equation through the forcing term. The cable response is then fed back in to the CML through the amplitude term $K^k$. It seems appropriate that the $Y^k$ output of the wave equation

(giving the cable shape) could be used directly in the CML. However, in order to incorporate some flexibility in the model, a linear gain factor $G$ will be included, giving

$$K^k = GY^k. \tag{2.90}$$

Again, the $G$ in Equation 2.90 is a free parameter, and its value will be set so as to match other simulations. Using the arguments presented above, the final set of equations for the coupled CML becomes

$$\begin{aligned}
f_n^k &= \frac{2C_l}{\pi\rho}\left[\sin(2\pi\theta_{n_1}^k - \phi_2^k) - \sin(2\pi\theta_{n_2}^k - \phi_2^k)\right], && (2.91)\\
\theta_{n+1}^k &= (1-2\epsilon)F_n^k + \epsilon(F_n^{k+1} + F_n^{k-1}), && (2.92)\\
F_n^k &= \theta_n^k + \Omega - \frac{(GY_n^k)}{2\pi}\sin\left[2\pi\theta_n^k - \phi_1^k - \frac{\pi}{2}\right] && (2.93)\\
Y_{n+1}^k &= 2Y_n^k - Y_{n-1}^k + c^2\frac{\Delta t^2}{\Delta z^2}(Y^{k-1} - 2Y^k + Y^{k+1})_n + f_n^k && (2.94)
\end{aligned}$$

### 2.3.3 Stability Concerns

The mid-point leapfrog finite difference scheme employed for the solution of the wave equation has the stability requirement that

$$\nu = c\frac{\Delta t}{\Delta z} \leq 1. \tag{2.95}$$

Recalling that the CML implies that the system is strobed at the excitation frequency, such that

$$\Delta t = \frac{1}{f_e}, \tag{2.96}$$

where $f_e$ was the forced excitation frequency of the cable. This is the inherent time step implied by the circle map in the CML. The $f_e$ term is now replaced with $f_n$, the natural vibration frequency of the cable. Recalling that the frequency ratio $\Omega$ is defined as

$$\Omega = \frac{f_{so}}{f_n} = \frac{\omega_{so}}{\omega_n}, \tag{2.97}$$

$\Delta t$ (non-dimensional) can be re-written as

$$\begin{aligned} \Delta t &= \frac{\Omega}{f_{so}} && (2.98) \\ &= \frac{\Omega}{St}. && (2.99) \end{aligned}$$

In this substitution, $f_{so}$ is the shedding frequency in the absence of cable vibration and is equal to the Strouhal number (recall that all variables have been non-dimensionalized).

The wave speed $c$ is set such that the $n$th mode of oscillation is in a lock-on condition. Using the definition of $\Omega$ above and the cable natural frequencies from Equation 2.89,

$$\begin{aligned} \Omega &= \frac{\omega_{so}}{\omega_n}, && (2.100) \\ \frac{n\pi c}{AR}\Omega &= 2\pi St, && (2.101) \\ c &= \frac{2StAR}{n\Omega}. && (2.102) \end{aligned}$$

Finally, $\Delta z$ is determined from the cable length $AR$ and the number of spatial nodes, $k^*$,

$$\Delta z = \frac{AR}{k^*}. \tag{2.103}$$

Returning to the stability requirement and combining Equations 2.99, 2.102, 2.103,

$$\begin{aligned} \nu &\leq 1 && (2.104)\\ c\frac{\Delta t}{\Delta z} &\leq 1 && (2.105)\\ \frac{2StAR}{n\Omega}\frac{\Omega}{St}\frac{k^*}{AR} &\leq 1 && (2.106)\\ \frac{2k^*}{n} &\leq 1. && (2.107) \end{aligned}$$

Typical values for the number of spatial nodes are on the order of $10^2$. This gives a clear stability problem. Thus, in order to be able to get stable solutions out of the wave equation, it must be sub-iterated at a small enough time step in order to satisfy Equation 2.95.

To minimize the number of sub-iterations, the time step for the wave equation will be set such that the stability parameter $\nu = 1$. The time interval of the wave equation, $\Delta t_w$, is defined in terms of the global time step $\Delta t$ and the number of sub-iterations necessary to satisfy the stability requirement, $N$:

$$\Delta t_w = \frac{\Delta t}{N} \tag{2.108}$$

Equation 2.95 becomes

$$\frac{c\Delta t}{N\Delta z} \leq 1. \tag{2.109}$$

Following the stability arguments above, this becomes

$$\frac{2k^*}{Nn} \leq 1. \tag{2.110}$$

Thus, in order to have the stability parameter $\nu = 1$,

$$N = \frac{2k^*}{n}. \tag{2.111}$$

Equation 2.111 specifies the number of required time steps in the sub-iteration of the wave equation (for each global time step) in terms of the number of oscillators $k^*$ and the wave number $n$ in order for the finite difference solution algorithm to be stable.

## 2.4 Algorithm for Solution of Coupled System

The previous section yielded a stability restriction on the wave equation. The end result of this restriction is that the time step inherent in the circle map (and therefore the CML that is responsible for modeling the wake dynamics) is too large in order to get stable solutions out of the wave equation.

The basic solution strategy in dealing with the coupled system is to sub-iterate the wave equation inside the CML time step. This introduces a new problem in terms of dealing with the $\theta$ output from the CML. The phases of vortex shedding ($\theta$) from the two shear layers act as inputs to the forcing term of in the wave equation. Fundamentally, the $\theta$ output of the sine circle map is a discrete quantity; it is the result of strobing the dynamics at the excitation frequency. Strictly speaking, values of $\theta$ at time levels within the forcing cycle are not defined. Thus it is necessary to interpolate their values at the sub-time levels used in the solution of the wave equation. A simple linear interpolation is performed to account for this problem.

Recall that $\theta_n^k$ is taken to be the phase of vortex shedding value at the $n$ time level and $k$ spatial node. From the stability requirements, there will be $N$ sub-time intervals within the wave equation. Let $\theta_{n_i}^k$ be the $\theta$ value at global time step $n$, sub-time step $i$, and spatial node $k$. Using a linear interpolation, its value becomes

$$\theta_{n_i}^k = (\theta_{n+1}^k - \theta_n^k)\frac{i}{N} + \theta_n^k. \tag{2.112}$$

It is this value of $\theta_n^k$ that is calculated at each sub time interval and then plugged in to the wave equation (Equation 2.94).

The methodology employed in the solution of the system of coupled equations (Equations 2.91 - 2.94) is depicted in the flow chart of Figure 2.9.

The inputs to the system are the initial conditions for the wake and cable ($Y_0^k$, $\theta_0^k$), the frequency ratio ($\Omega^k$), and the two free parameters ($K_0$ and $C_l$). This information is fed in to the CML wake model, which calculates the wake parameters at the next time step. The wake data then goes in to the wave equation finite difference algorithm. After first performing a linear interpolation between $\theta_n$ and $\theta_{n+1}$ over $N$ sub time steps, the cable displacement at each sub-time level is calculated. The final values for cable displacement ($Y_{n+1}^k$) is then returned to the CML. This process is iterated until both the wake and cable motion achieve steady-state, time-periodic solutions. The outputs of the map are the motion of the cable and the wake pattern, $\theta_n^k$.

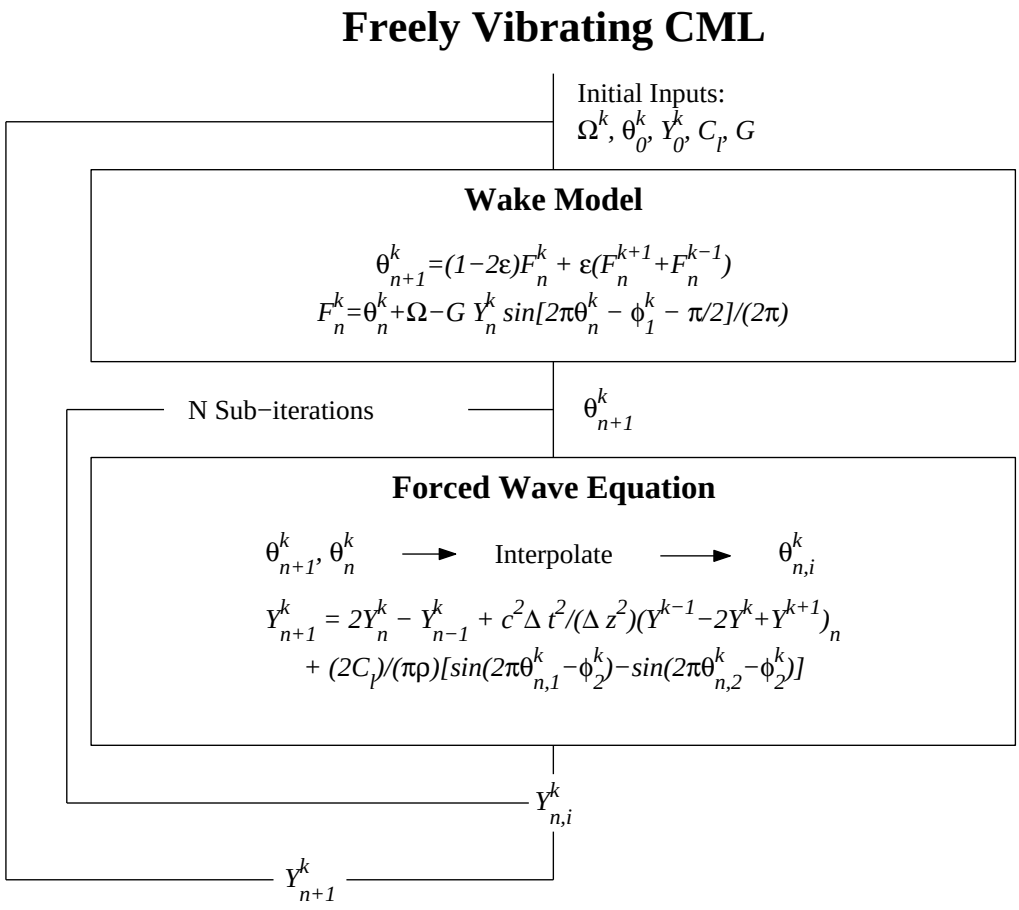


Figure 2.9: Flow Diagram for CML Solution Algorithm

# Chapter 3

# Results

## 3.1 Results for 2-D Simulations

The successful simulation of a two dimensional rigid oscillating cylinder model is a necessary first step before endeavoring to tackle the more complicated three dimensional wave equation. By gaining valuable insight into the behavior of the elastically mounted cylinder, the algorithm can be refined and tuned in preparation for solving the flexible cable problem.

Perhaps most important before examing results is the proper tuning of the free parameters $C_l$ and $G$. This is done through matching the maximum crossflow displacement in a one to one lock in condition (that is, $\Omega = 1$) to values from the CFD simulations of Newman. For 2-D cylinder results, Newman reports a crossflow amplitude of around $y = 0.5$ (recall that all length variables are non-dimensionalized by cylinder diameter). The cylinder mass ratio $\rho$, and damping ratio $\zeta$ are set to values similar to this study as well. The natural frequency $\omega_n$ is tuned according to the cylinder Strouhal frequency and the particular $\Omega$ value of the study, and is given by

$$\omega_n = \frac{2\pi St}{\Omega}. \tag{3.1}$$

All that remains is to tune $C_l$ and $G$. Through the conduction of a parametric study where both $C_l$ and $G$ were varied over wide ranges, the values were found that gave the desired match in displacement amplitude. Figure 3.1 is a contour plot showing the resulting maximum displacement amplitude predicted by the model for various combinations of $C_l$ and $G$.

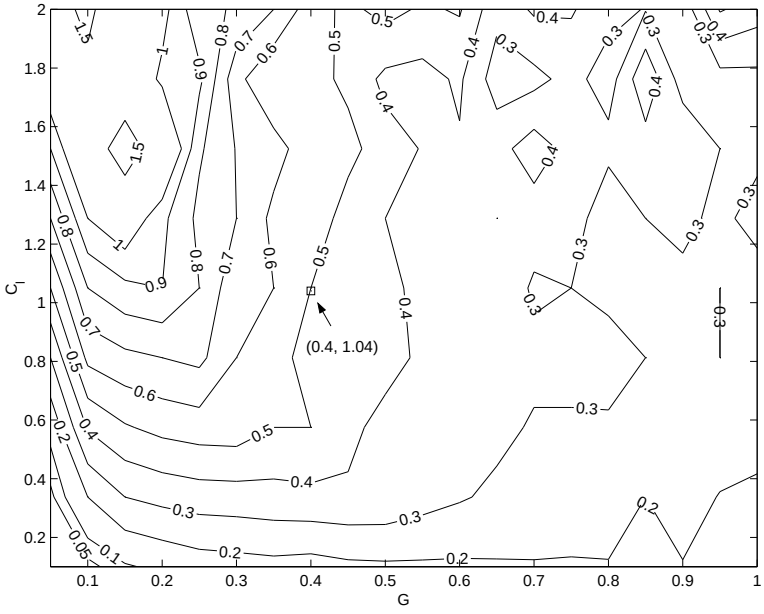


Figure 3.1: Contours of Maximum Amplitude for Various $C_l$ and $G$ Combinations

Notice that there is not one unique combination of $C_l$ and $G$ that will give the desired amplitude of $y = 0.5$. The combination of free parameters that were found to give the best results were $G = 0.4$, $C_1 = 1.04$. The value of $C_l$ is on the order of one, which compares favorably to the lift coefficient values reported by Newman and Karniadakis [15]. All of the input parameters for the study are summarized in Table 3.1.

| Parameter | Value |
|---|---|
| $\rho$ | 2 |
| $\zeta$ | 0.01 |
| $\omega_n$ | $2\pi St/\Omega$ |
| $C_l$ | 1.04 |
| $G$ | 0.4 |

Table 3.1: Input Parameters to 2-D Coupled Map

### 3.1.1 Results for $\Omega = 1$

The crossflow displacement $y$ time history for the $\Omega = 1$ (1/1 lock on condition) can be seen in Figure 3.2. The cylinder oscillates in a regular sinusoidal manner, with increasing amplitude until it reaches a steady-state value of $y = 0.5$. Recall that $C_l$ and $K_o$ were chosen to give this result. The frequency at which the cylinder is vibrating can be determined by examining the frequency spectrum of its motion. This result is presented in Figure 3.3. Not surprisingly, there is a clear spike at $\omega/\omega_{so} = 1$, showing that the cylinder is vibrating at the Strouhal frequency. With $\omega_n$ tuned to match the Strouhal frequency, a perfect lock on resonance condition is established and the cylinder vibrates at the same frequency as the wake.

It is important to recall that the circle map is only capable of predicting steady state behavior. While it is tempting to look at the results presented in Figure 3.2 as conveying the transient, start up behavior of an elastically mounted cylinder suddenly exposed to a uniform free-stream, that would be an incorrect interpretation. In this regard, the circle map model is simply predicting the sinusoidal nature and maximum amplitude of the response once it self-limits and oscillates at a steady amplitude. This is occurring after roughly 70 non-dimensional time units.

As a further illustration of the system settling out to a steady state, consider the results presented in Figure 3.4. Here, the $\theta$ iterates for both shear layers are presented as functions of iteration number, $n$.

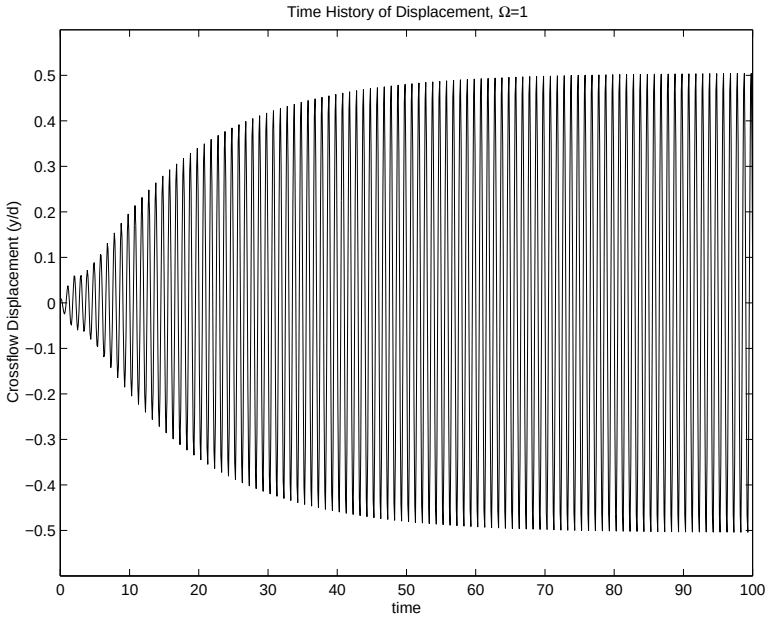


Figure 3.2: Crossflow Displacement vs. Time, $\Omega = 1$

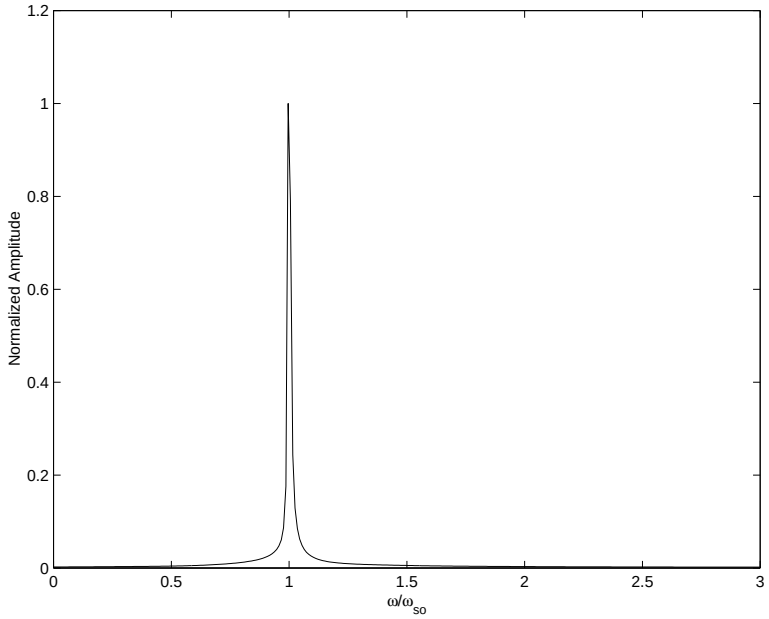


Figure 3.3: Frequency Spectrum of Crossflow Displacement, $\Omega = 1$

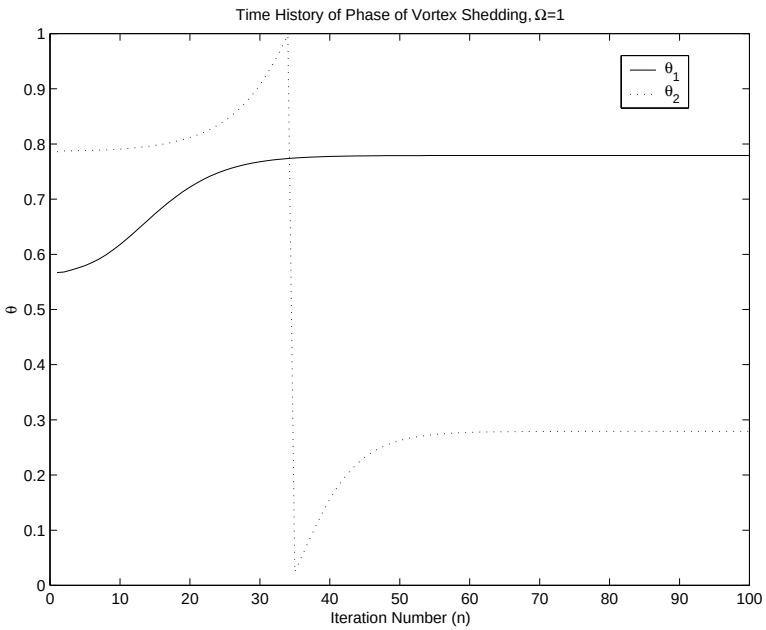


Figure 3.4: Phase of Vortex Shedding ($\theta$) vs. Iteration Level

The initial conditions for the two shear layers are random (within the range $0 < \theta_o < 1$). After approximately 65 iterations, the values have achieved their steady state values. The steady state levels on $\theta_1$ and $\theta_2$ are exactly $\Delta\theta = 0.5$ apart. Recall that $\theta$ is defined modulo $2\pi$; the $\Delta\theta = 0.5$ is a result of the model specifying that the two shear layers be 180° out of phase with one another. By predicting constant steady state values on the phases of vortex shedding of the two shear layers that are separated by a $\pi$ phase difference, the model is effectively describing the alternating wake behind the cylinder with regularly spaced, parallel vortex filaments. This result is consistent with the NEKTAR studies of Newman and Karniadakis.

### 3.1.2 Results for $\Omega \neq 1$

Now the value of $\Omega$ will be varied to examine the response of the cylinder in non lock-on conditions. Physically, the modifying of $\Omega$ is akin to changing the natural frequency of the cylinder. This moves the natural frequency away from the stationary shedding frequency, altering the resonance condition of the $\Omega = 1$ case.

Figures 3.5 and 3.6 plot the maximum amplitude of cylinder displacement and its vibration frequency as a function of the cylinder's natural frequency. The x-axis is normalized by the stationary shedding frequency of the cylinder, $\omega_{so}$. This ratio is then equal to the inverse of $\Omega$.

From Figure 3.5, it is clear that the maximum cylinder displacement occurs in the neighborhood of $1/\Omega = 1$, and drops off in level on either side. The largest cylinder motions are occurring in the envelope $0.9 \leq 1/\Omega \leq 1.0$, that is, when the natural frequency is at or slightly lower than the Strouhal frequency. Far away from the Strouhal frequency, the amplitudes become much smaller as the resonance effect coupling the fluid forcing to the cylinder's natural frequency is lost. It is interesting to observe that the maximum cylinder displacement occurs at a value of $1/\Omega = 0.91$ ($\Omega = 1.1$). The occurrence of a maximum amplitude response at a frequency ratio other than $\Omega = 1$ is a characteristic of a self-induced oscillator.

While the general shape of this curve is consistent with the NEKTAR results, there are some notable differences. The NEKTAR curve shows a peak in amplitude at a value of $\omega_n$ slightly *greater* than 1, and a slightly broader plateau over which significant displacements occur. The maximum crossflow displacement, while occurring at different values of $\omega_n$, is consistent between the two studies.

Turning to Figure 3.6, there is a clear linear relationship between the frequency at which the cylinder vibrates and the natural frequency of the cylinder. Quite simply, the cylinder is vibrating at its natural frequency across the entire range of

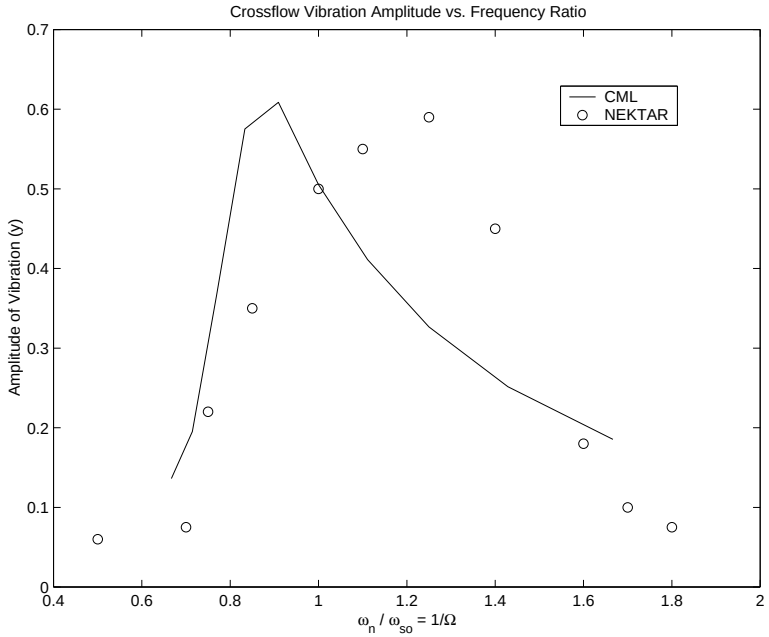


Figure 3.5: Maximum Amplitude of Cylinder Motion vs. Natural Frequency

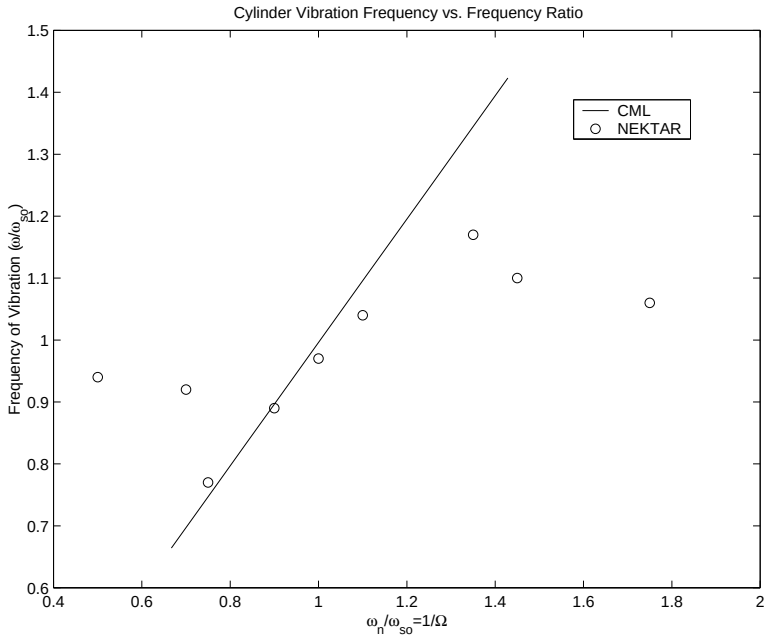


Figure 3.6: Frequency of Cylinder Vibration vs. Natural Frequency

$\Omega$ presented. This is a result of the shedding frequency of the vortices adjusting to the natural frequency of the cylinder, as classic lock-on condition. The NEKTAR results show a clear linear range (lock-on) around $1/\Omega = 1$, outside of which the cylinder vibration frequency trends towards the shedding frequency of the cylinder. The CML model is incapable of picking up this behavior. Closer examination of the CML results in the $\Omega$ range outside of which the NEKTAR results show a linear relationship yields some insight in to why this is so.

Consider Figures 3.7 and 3.8. Here are plotted the displacement time history and frequency spectrum for the case where $\Omega = 1.5$ ($1/\Omega = 0.67$). The NEKTAR results at this frequency ratio show the frequency of vibration trending towards the shedding frequency of the cylinder. The CML results are contradictory, seeming to indicate that the cylinder is still in the linear lock-on regime.

From Figure 3.7, the vibration of the cylinder is seen to be erratic. No longer does the cylinder vibrate at a pure sinusoid of a single frequency. Turning to the frequency spectrum (Figure 3.8), it is clearly seen the presence of additional harmonics. The strongest peak is at the natural frequency, continuing the linear progression. However, for the first time there is a substantial peak at the shedding frequency ($\omega/\omega_{so} = 1$). There is also some frequency content at a subharmonic of the natural frequency. Thus, while the cylinder vibrates primarily at its natural frequency, its nature is considerably more complex than it is at any of the other frequency ratios within the linear range predicted by NEKTAR. The CML is beginning to pick up this more complex behavior, but is still unable to match the NEKTAR predictions.

This demonstrates some of the limitations of the CML approach: at frequency ratios close to one, the dynamics are simple enough that the CML is able to successfully model certain aspects of the cylinder response. At non-resonance conditions, however, the CML's simplicity is its downfall, and it is clear that there are addi-

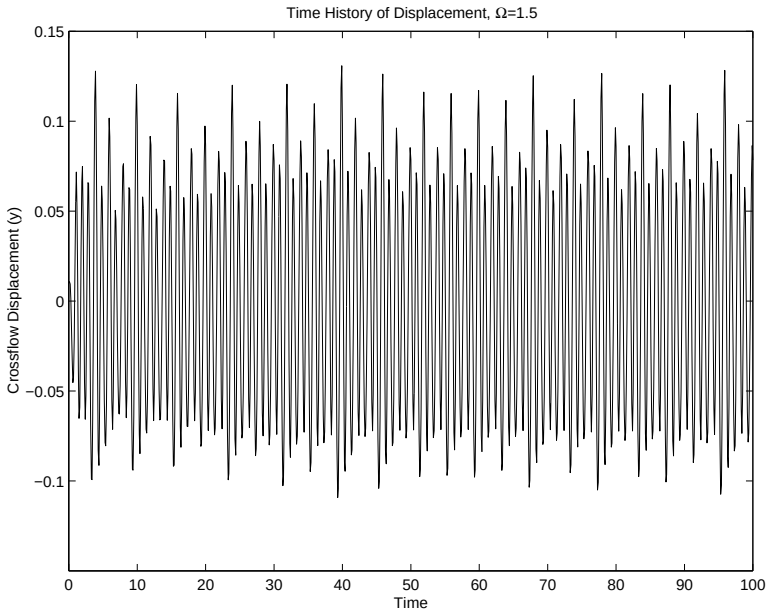


Figure 3.7: Cylinder Displacement vs. Time, $\Omega = 1.5$

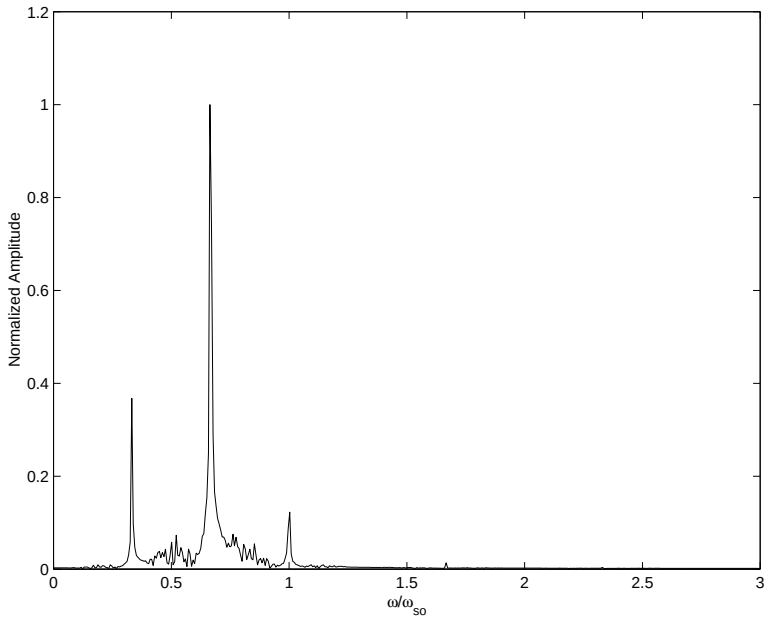


Figure 3.8: Frequency Spectrum of Cylinder Displacement, $\Omega = 1.5$

tional dynamics that are not being unmodeled. The introduction of self-learning techniques into the CML, that would be capable of better tuning the free parameters of the map online, most likely would improve the ability of the CML to predict and match the NEKTAR results. This might also provide an explanation for the shift in the peak of the amplitude plot (Figure 3.5).

## 3.2 Results for 3-D CML Model

Using the insight gained through the tuning of the two dimensional model, the CML - Wave Equation 3-D model was studied. The values of the free parameters $C_l$ and $G$ determined in the rigid cylinder model were used as starting points for to set initial values in the cable model. It was initially postulated that the values of $C_l$ and $G$ presented in Table 3.1 would properly tune the 3-D cable model. This was not found to be the case, however, and the free parameter values used in the flexible cable problem were drastically different to those in Table 3.1. Again, the criteria for arriving at the chosen values was the matching of maximum crossflow amplitudes to those reported by Newman and Karniadakis [15] for the resonance case at $\Omega = 1$. The final input parameters for the baseline case of a second mode standing wave cable response are presented in Table 3.2. Recall that in the flexible cable model, in order to tune mode $n$ to the Strouhal frequency, the wave speed $c$ is set to

$$c = \frac{2StAR}{n\Omega}. \tag{3.2}$$

From the Table, the value of $C_l$ used in the three dimensional simulations is seen to be roughly an order of magnitude smaller than its value in the two-dimensional simulations. The value of $G$, meanwhile, remains order one.

| Parameter | Value |
|---|---|
| $\rho$ | 2 |
| $\zeta$ | 0.01 |
| $c$ | $2StAR/(n\Omega)$ |
| $AR$ | 25 |
| $C_l$ | 0.08 |
| $G$ | 1.0 |

Table 3.2: Input Parameters to 3-D Coupled Map

### 3.2.1 Second Mode Standing Wave, $\Omega = 1$

The baseline condition that was studied is that of a second mode standing wave cable response at resonance ($\Omega = 1$). While in the forced (uncoupled) CML algorithm, the amplitude and mode shape would be input directly in the model, the goal in the freely vibrating CML is to set boundary conditions such that a second mode standing wave is the resultant output of the wave equation model, not the input response. The map is then iterated and the actual cable motion is determined.

The primary step in the initialization of the problem is setting the cable tension through the wave speed, $c$, as described in Equation 3.2. With the tension tuned to a second mode ($n = 2$) and with pinned boundary conditions on the cable ends, the favored response is a standing wave. The initial conditions on the cable displacement along the span are random (excluding the pinned conditions at $y = 0$ and $y = AR$). In addition, the initial distribution of both $\theta^k_{0_1}$ and $\theta^k_{0_2}$ (phase of vortex shedding) along the cable span are random. It is important to remember that the model proposed seeks to predict the *steady state* nature of both the cable motion and resulting wake pattern. Using random initial conditions on both the wake and cable motion are important to demonstrate the validity and robustness of the algorithm.

### Cable Response

Figure 3.9 shows the time evolution of the motion of the cable at an anti-node. The behavior of the motion is very similar to the results found for the 2-D case; the motion is a regular sinusoid of increasing amplitude until a steady state displacement is reached. The steady state maximum displacement is the value used to tune the free parameters $C_l$ and $G$. The anti-node is chosen as the comparison point because it represents the location of maximum displacement across the cable span. For a standing wave response in a flexible cable, Newman and Karniadakis report a maximum crossflow displacement of $y = 0.69$. This is the value that is matched in these simulations, as can be seen from the steady state amplitude presented in Figure 3.9.

It is clear that the anti-node location appears to be behaving as if it were in a standing mode response. Furthermore, its response in the frequency domain can be examined through the frequency spectrum of the anti-node cable displacement, which is presented in Figure 3.10. The cable is vibrating at its natural frequency, which is clearly verified by the sharp peak at $\omega/\omega_2 = 1$, where $\omega_2$ is the second natural frequency of the cable.

To verify that the entire cable is vibrating in a self-excited standing wave - recall that the initial conditions were random, potentially exciting *all* modes of the cable - the cable shape ($y$ amplitude vs. spanwise location at several discrete values of time) is plotted in Figure 3.11

The regular, standing wave motion of the cable can clearly be seen. This is a crucial result: with the cable tension set so as to match the second structural natural frequency to the stationary cylinder shedding frequency, the model predicts a standing wave cable motion with random initial conditions placed on both the cable motion and the wake structure.

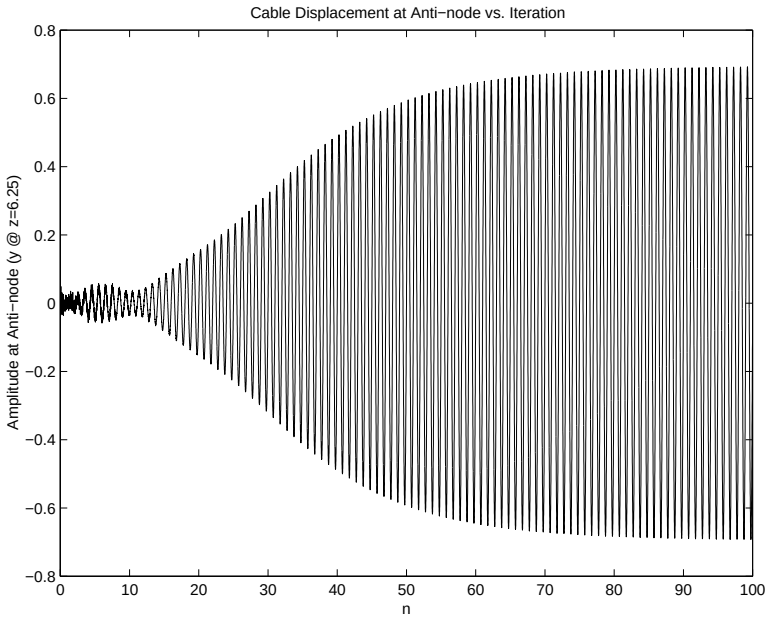


Figure 3.9: Cable Displacement at Anti-node

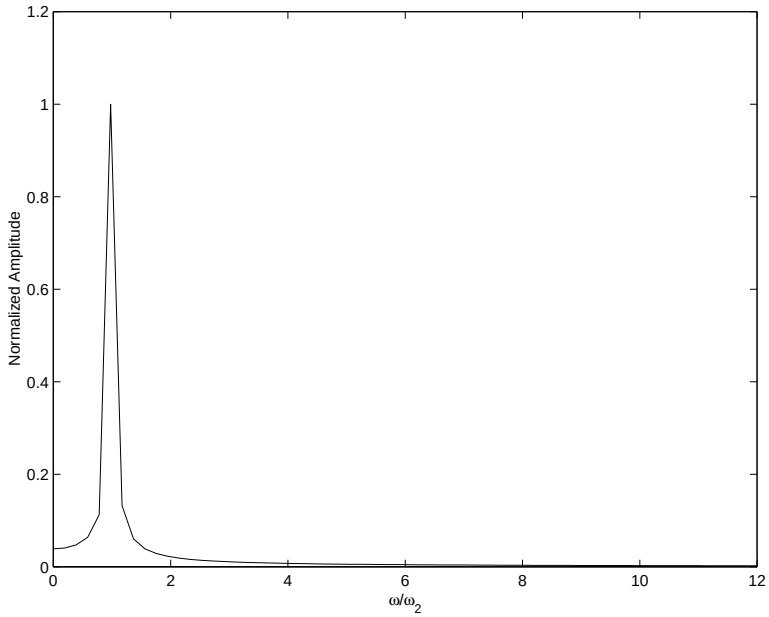


Figure 3.10: Frequency Spectrum of Cable Displacement at Anti-node

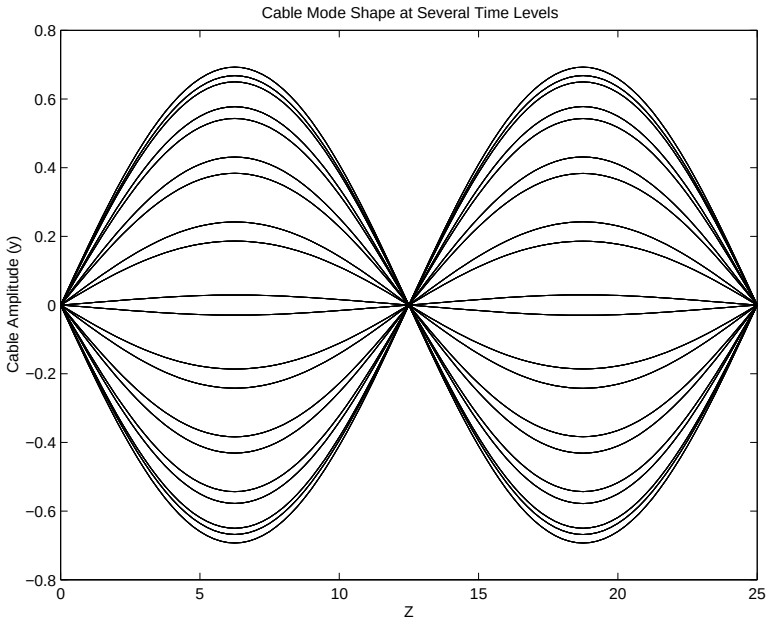


Figure 3.11: Cable Shape at Different Time Values, $\Omega = 1$

To understand why this occurs, it is helpful to examine the forcing time history and frequency spectrum. Figures 3.12 and 3.13 present the time history and frequency spectrum of the forcing term in the wave equation at the cable anti-node.

At first glance, the time behavior of the cable forcing looks remarkably similar to the cable displacement; the forcing starts from a low level and increases in amplitude until a steady state is reached. The frequency of the forcing is also similar to that of the cable motion, showing the same characteristic spike at $\omega/\omega_2 = 1$ representing perfect 1/1 lock on conditions. These results are the direct consequence of the specification of $\Omega = 1$ everywhere along the cable span as well as the linearization of $\theta$ across each shedding cycle. With the cable forcing occurring at a frequency identical to the natural frequency of the cable mode to which the wave speed was set, it is not surprising that a regular standing wave cable response results.

A brief summary of the results for $\Omega = 1$ standing wave lock-on cable responses will now be given. After specifying random initial conditions on the cable and

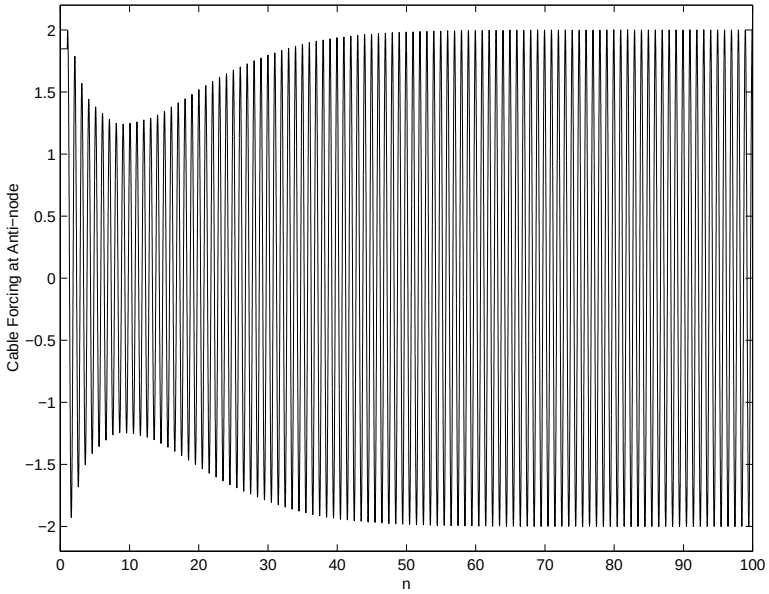


Figure 3.12: Time History of Forcing Term at Cable Anti-node

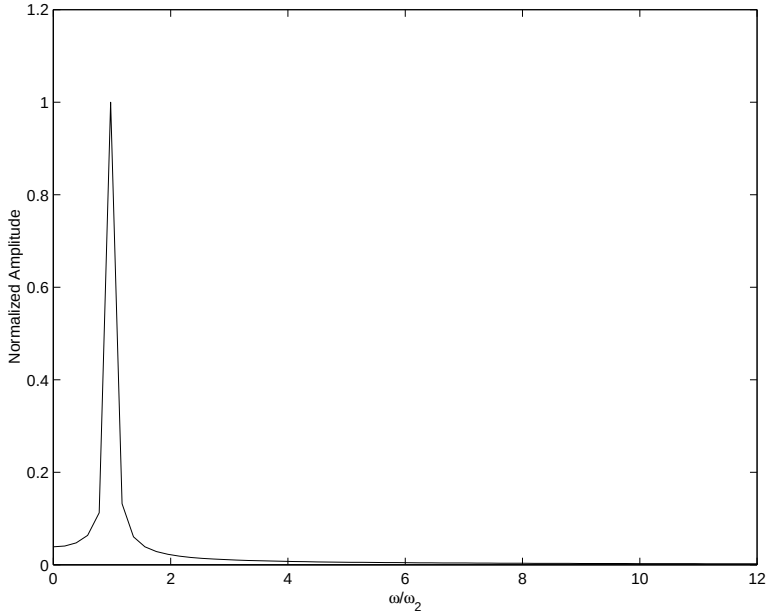


Figure 3.13: Frequency Spectrum of Cable Forcing at Cable Anti-node

setting the wave speed such that the second mode is in a $\Omega = 1$ lock on condition, a steady-state standing wave cable response results. While slightly different in implementation, this result is nearly identical to the CFD studies of Newman and Karniadakis. Rather than pinning the cable ends, they utilize periodic boundary conditions, allowing for either standing or traveling wave responses of the flexible cable. In their simulations, a standing or traveling wave response is set by setting the appropriate initial conditions on cable amplitude and velocity to the desired mode (or wavelength for traveling waves). They then report that all simulations converge to time-periodic cable responses within roughly ten vortex shedding cycles.

The CML method does not have the advantage of being able to study transient, start-up vibration behavior. Consequently, the number of shedding cycles to achieve a steady state cable motion (roughly 100 cycles in the results presented above) will not have any practical meaning. However, by properly tuning $C_l$ and $K_o$ to match amplitudes, the converged solutions between the two models will yield nearly identical results for the cable motion.

**Wake Patterns**

The distribution of the phase of vortex shedding for the two shear layers provides the best insight in to the wake dynamics. Previously, in the 2-D case, it was shown that after a certain number of iterations the phase of vortex shedding ($\theta$) reached a steady state value. In addition, the two shear layers were shown to be 180° apart in their shedding cycles. This demonstrated that the wake was in a 1/1 lock-on condition and that the two shear layers were alternating in the wake shedding cycle (familiar Karman vortex street).

Figure 3.14 shows the companion scenario for the 3-D case. The evolution of both $\theta^k_{n_1}$ and $\theta^k_{n_2}$ is shown at the first anti-node (z=6.25). Again, the $\theta$ values evolve

from a random initial value to achieve a constant steady-state, indicative of the 1/1 lock-on condition. Comparing the steady state values of the two shear layers, it is again noted that their values differ by 0.5, denoting the 180° phase shift between shear layers.

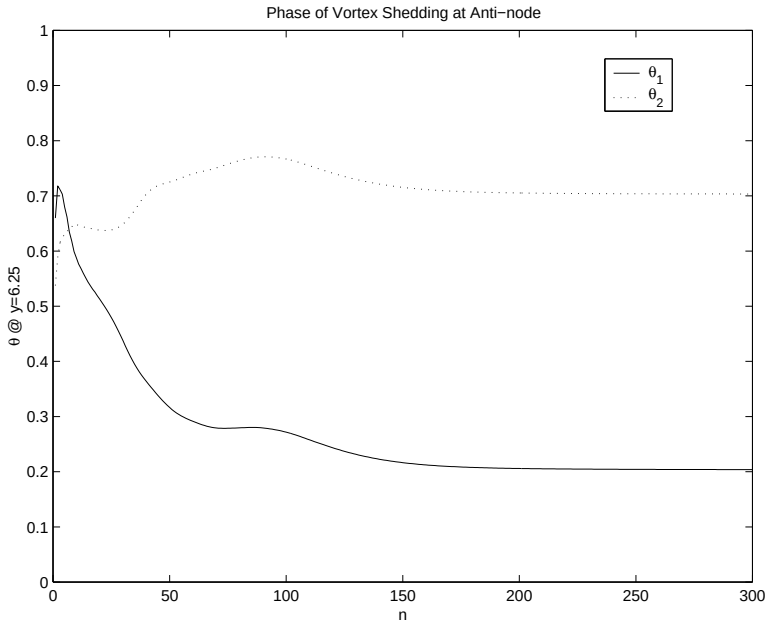


Figure 3.14: Time History of $\theta$ at Anti-node

It would appear that at the anti-node the wake is behaving in an identical fashion to the 2-D rigid cylinder wake. This is not the case at other spanwise locations.

By extending the model to a third dimension, $\theta_n^k$ now becomes a function of spanwise position, yielding the vortex shedding wake patterns discussed earlier. Vorticity is diffused in the spanwise direction yielding differences in the vortex core location along the span of the cable. The parameter $\theta_n^k$ for the $\Omega = 1$, second mode standing wave cable motion condition is presented in Figure 3.15. The values plotted are the final, steady-state results. At locations away from the anti-nodes, the two shear layers cease to be 180° out of phase.

Rather than having a constant $\Delta\theta$ along the cable span denoting vortex filaments

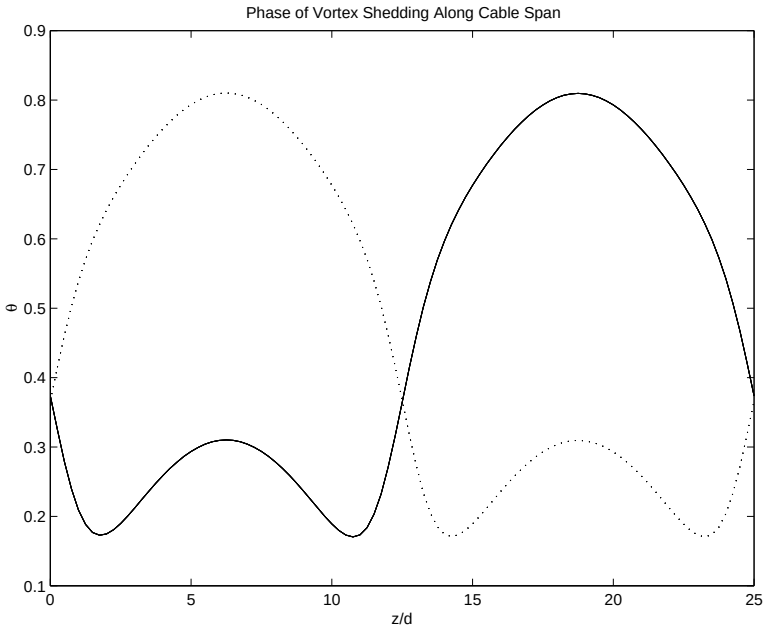


Figure 3.15: Phase of Vortex Shedding Distribution, $\Omega = 1$

that are parallel (as in the rigid cylinder case), the two $\theta_n^k$ distributions are seen to interweave with one another in what is termed a *lace-like* wake structure. Lace-like structures have been observed in numerical simulations of flexible cables [15], [14], and in experiments [12]. Comparisons between the CML results and the numerical NEKTAR results will be discussed in subsequent sections. In converting the results of Figure 3.15 to a wake pattern in the manner discussed earlier, a streamwise shift needs to be applied to the second shear layer, as discussed in Section 2.3.

A better method of visualizing the wake is by plotting the vortex core locations. Figure 3.16 is a three-dimensional representation of the entire cable - wake interaction.

The cable is free to vibrate in the $y$ - $z$ plane. The second mode standing wave response is clearly evident. Several vortex filaments are shown as they evolve in the $x$ - $z$ plane. The two different shear layers are denoted by the open and closed circles, marking the discrete location of the vortex cores. Note the streamwise shift applied

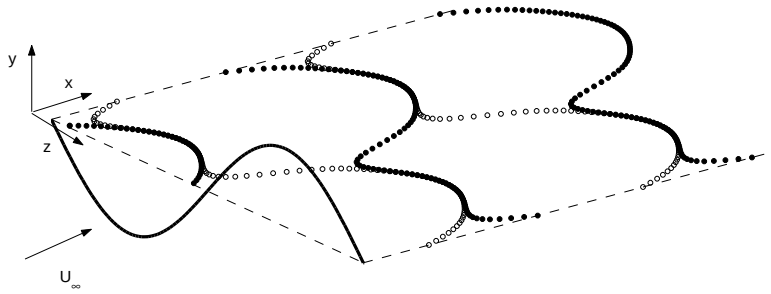


Figure 3.16: Lace-like Wave Pattern, $\Omega = 1$

to the second shear layer, such that the "M" shaped profile at the anti-node of one shear layer overlaps the peak of the other shear layer. This shows that the vortices from the two shear layers are shedding simultaneously at the anti-nodes. At cable nodes, the vortices are shed alternately, as in the 2-D cylinder wake. This shedding behavior, symmetric at cable anti-nodes, and alternate at nodes, is responsible for the lace-like nature of the wake pattern.

### 3.2.2 Second Mode Standing Wave, $\Omega \neq 1$

It is now desired to examine the case when the natural frequency of the cable is near, but slightly different from, the stationary vortex shedding frequency of the cable. Presented in Figure 3.17 is the companion figure to Figure 3.16, for the case where $\Omega = 0.99$.

By closely examining the figure, it appears that in the region of cable anti-nodes, the wake is reasonably ordered and resembles a lace-like pattern. At nodes, however, the wake appears to be randomly distributed, with dislocations in the vortex core locations.

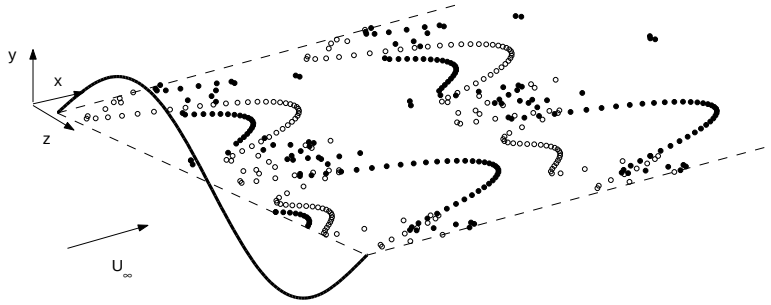


Figure 3.17: Wake Pattern Showing Vortex Dislocations, $\Omega = 0.99$

To see how this effects the cable vibration, consider Figure 3.18. Here are plotted the cable mode shape at several snapshots of time. As in the $\Omega = 1$ case, the cable is vibrating in a standing mode shape. Also as before, the cable is vibrating at its natural frequency. Indeed, the majority of the results for the behavior of the cable vibration is the same for $\Omega = 0.99$ as it is for $\Omega = 1.0$. There are some notable differences, however.

Perhaps most notable is that there is an asymmetry in the vibration. The amplitude level at one anti-node is slightly larger than at the other. The maximum cross-flow vibration amplitude is $y = 0.66$, which is just slightly lower than the value of $y = 0.68$ for $\Omega = 1$. Also apparent in the figure is that the cable vibration in the neighborhood of the node is slightly irregular. For the $\Omega = 1$ case, the amplitude at half the cable span (the location of the node) was always strictly zero. Now, the cable is showing some level of vibration at mid-span, and the node is drifting left or right of the center just slightly, indicating the presence of a small traveling wave response. It is not surprising that the vibration at the nodes be somewhat irregular, given the complexity of the wake and the dislocations in the wake pattern in the

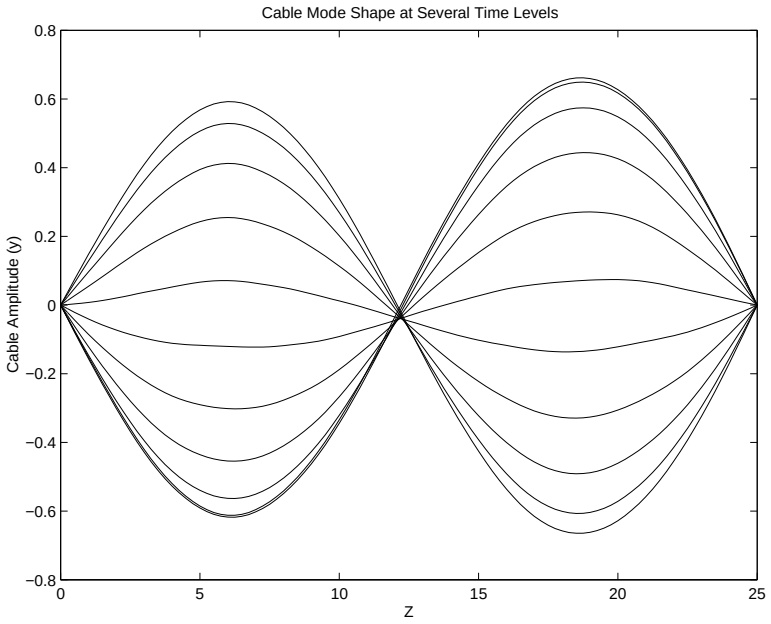


Figure 3.18: Cable Shape at Several Time Levels, $\Omega = 0.99$

vicinity.

A possible explanation for the presence of the dislocations in the wake near cable nodes requires returning to the amplitude-frequency (K - $\Omega$) plane for the sine circle map, Figure 2.3. Olinger [18] notes that while two dimensional, rigid cylinder results can be explained by considering only a single point in the amplitude - frequency plane, flexible cable results require consideration of several points, due to the fact that different cable locations are vibrating at different amplitudes.

When $\Omega = 1$, all amplitude ($K$) levels fall within the 1/1 lock-on regime. Thus, the lock-on condition is the same at all spanwise cable locations, and the wake remains ordered with out the presence of dislocations, since a vortex dislocation would indicate that neighboring spanwise cable locations were shedding vorticies at drastically different frequencies.

Consider now moving away from the $\Omega = 1$ lock-on case. This corresponds to moving laterally on the frequency ($\Omega$) axis of Figure 2.3. Drawing a vertical line

from at a particular frequency value shows that different amplitude levels fall within different lock-on tongues. This sets up the possibility of having several different lock-on conditions along the cable span, as different $z$ locations vibrate at different amplitudes in the standing wave cable motion.

Return now to the $\Omega = 0.99$ case. At low amplitude levels (near cable nodes), the circle map (and therefore the CML wake model) is in a quasi-periodic state on the amplitude - frequency plane. Indeed, it is near the cable nodes where the complex wake behavior and vortex locations occur. Alternatively, at higher amplitude values (near anti-nodes), the wake remains in a 1/1 resonance state, and the wake is ordered similarly to the $\Omega = 1$ case.

### 3.2.3 Comparisons Between Freely Vibrating and Forced CML

It is now desired to summarize the major results of the freely vibrating CML model and make comparisons with both the earlier forced CML model of Olinger [18] and the NEKTAR simulations of Newman and Karniadakis [14], [15]. This is done in part to attempt to answer the fundamental question posed earlier - do forced and freely vibrating cables (at the same frequency and amplitude of vibration) exhibit identical wake structures? Already it has been shown that the two-dimensional freely vibrating model is capable of predicting some aspects of the NEKTAR results, particularly in the frequency region very close to $\Omega = 1$.

First comparisons will be made with the forced CML model [18]. In the forced CML model, the level of cable forcing and frequency are input directly in to the CML wake model, through the $K^k$ term and $\Omega$ from Equation 2.10. The $K^k$ term is calculated from Equation 2.13 which gives the desired mode and amplitude level. In order to match conditions between the models, the maximum amplitude level $K_0$

that will be input in to the forced CML will be set so as to match the product of the free parameter gain $G$ and the cable amplitude $y$ in the freely vibrating case. Recall that the results from the freely vibrating model were specifically set such that the maximum cable amplitude was $y = 0.68$. Also recall that $G = 1$. Using these two values, the appropriate value of $K_0$ for the forced CML is $K_0 = 0.68$.

Figure 3.19 plots the $\theta$ distributions for both the freely vibrating and forced models. For clarity, only a single shear layer is plotted. Qualitatively, the two shear layers show very similar $\theta$ distributions, with both predicting the characteristic "M" profile near cable anti-nodes. Some differences in the detailed phase angle distribution do exists, however, particularly near cable anti-nodes.

Once these $\theta_n^k$ distributions are converted to their corresponding wake patterns, they are virtually indistinguishable. The three-dimensional wake pattern view for the forced CML results are presented in Figure 3.20. The freely-vibrating wake pattern was presented in Figure 3.16, and no discernable differences are seen between the two. The two CML models predict nearly identical wakes.

In Figure 3.21 similar comparisons from CFD studies conducted by Newman and Karniadakis are presented. Repeated in the figure are Figures 5 and 6 from [14], showing contours of spanwise vorticity in the wakes of both freely vibrating (top) and forced (bottom) cable wakes. The flow is from left to right, with $x = 0$ denoting the location of the vibrating cable. The Reynolds number of the study is $Re = 100$, consistent with the Reynolds number of the CML results. The frequency ratio is also set to be in a 1/1 resonance condition ($\Omega = 1$), again consistent with the CML results presented.

While there are slight differences in the near wake structures, the two figures look very similar. The NEKTAR results confirm that at $Re = 100$, there is little difference between the wake of a freely vibrating cable and the wake of a forced

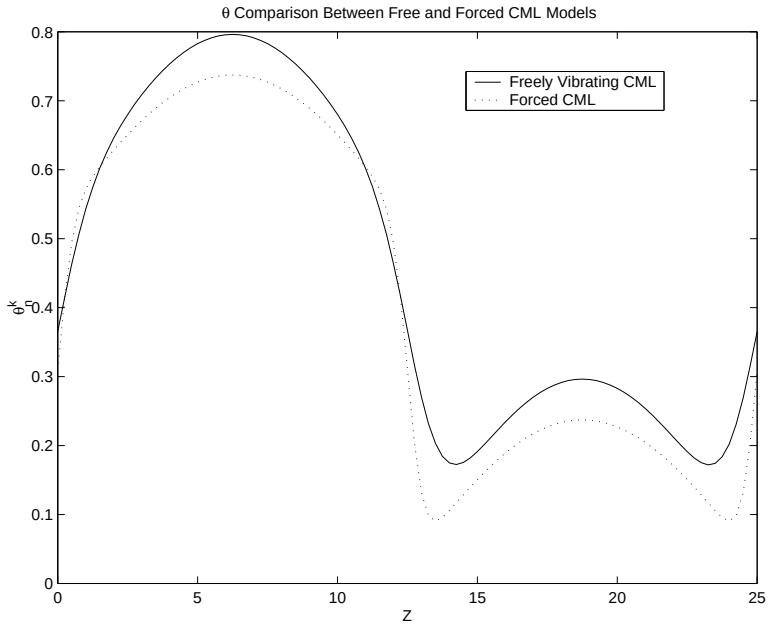


Figure 3.19: Comparison of the $\theta_n^k$ Distribution for the Freely Vibrating and Forced CML Models

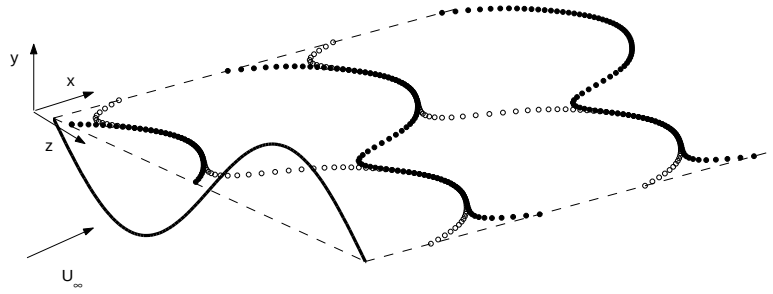


Figure 3.20: Wake Pattern for Forced CML Model, $\Omega = 1$

cable.

### 3.2.4 Comparisons Between Freely Vibrating CML and NEKTAR Simulations

The two figures from the NEKTAR study of Newman and Karniadakis (Figure 3.21) are also useful in making qualitative comparisons between the freely vibrating CML and NEKTAR.

In order to make these comparisons, it is first necessary to relate the CML wake patterns to the spanwise vorticity data output from NEKTAR. Recall that the $\theta_n^k$ parameter in the CML is directly related to spanwise vorticity. In the case of a rigid oscillating cylinder, all spanwise locations shed simultaneously and a parallel shedding pattern is observed. In terms of CML results, this is represented in the $\theta_n^k$ wake patterns by the vortex core filaments being parallel with one another. In terms of the spanwise vorticity contours of the NEKTAR results, parallel bands of vorticity would be observed.

Turn now to the freely vibrating cable results presented for $\Omega = 1$. The CML results are presented in Figure 3.16; NEKTAR results are shown in Figure 3.21a. One important difference between the two results is the cable shape; for the NEKTAR results, the cable anti-nodes are located at the two ends and directly in the middle (a cosine mode shape) of the span, while the CML results have anti-nodes at the one-quarter and three-quarted spanwise locations (a sine mode shape).

By tracing a particular vorticity band in the NEKTAR results, it is possible to create a schematic of the lace-like, interwoven structure. Tracing a specific vorticity contour in the NEKTAR plots is analogous to one of the vortex filaments in the CML results, Figure 3.16. This interpretation of the vortex structure has been added to Figure 3.21a, and was not present in the original figure from [14]. Comparing the

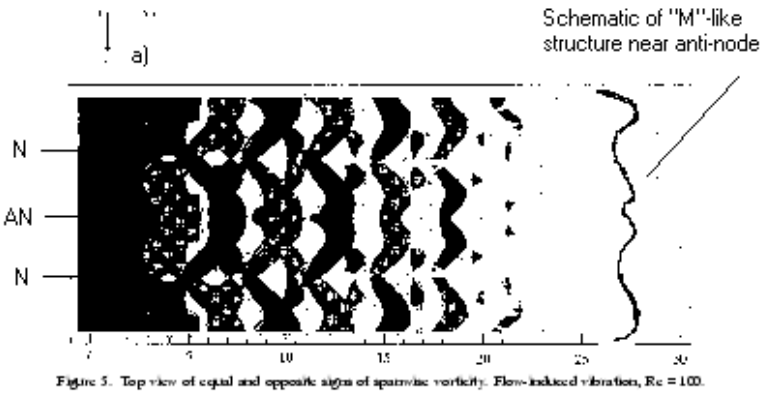


Figure 5. Top view of equal and opposite signs of spanwise vorticity. Flow-induced vibration, Re = 100.

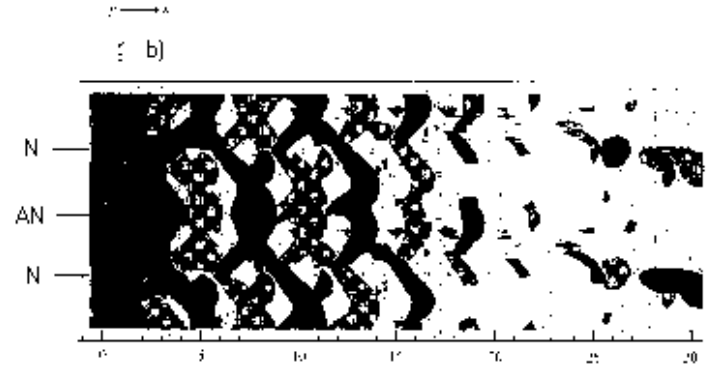


Figure 6. Top view of equal and opposite signs of spanwise vorticity. Forced vibration, Re = 100.

Figure 3.21: NEKTAR Vorticity Patterns for both Freely Vibrating and Forced Cable Wakes, from [15], Figures 5 and 6. Additional wake structure added in the present work, and is not found in [14]

structures near the anti-nodes of the two figures, both show an "M" like profile. This is further reassurance that, at least qualitatively, the freely vibrating CML is predicting similar wake structures to the more complex CFD models for the 1/1 lock on case presented.

One final comparison between the freely vibrating CML and the NEKTAR results will serve to summarize the global behavior of the amplitude response of flexible cables at lock-on conditions. Griffin [7] has proposed a universal curve that seems to govern their behavior. The relevant parameter affecting the amplitude response of flexible cables is the mass-damping (or response) parameter $S_G$, which is defined to be

$$S_G = 8\pi^2 St^2 \zeta_s \rho. \tag{3.3}$$

In Equation 3.3, $St$ is the Strouhal number, $\zeta_s$ is the structural damping, and $\rho$ is the ratio of cable mass to fluid mass. Essentially, $S_G$ represents the product of mass and damping for a given cable.

Plotted in Figure 3.22 is the maximum cable crossflow amplitude versus the mass-damping parameter $S_G$ for the freely vibrating CML and NEKTAR simulations. The results presented are for a mass ratio of $\rho = 1$. The freely vibrating CML is tuned (through the free parameters $C_l$ and $G$) to match the NEKTAR amplitude at the mass-damping value of $S_G = 0.01$. The mass-damping parameter was then varied (by changing $\zeta$) and the resulting amplitude of vibration determined and plotted. Since the model is tuned to match the NEKTAR results at $S_G = 0.01$, it can accurately predict vibration amplitude levels up to approximately $S_G = 0.1$, a full order of magnitude range in $S_G$.

The range of values of the mass damping parameter for typical marine cables is indicated on the figure. Within the marine cable range, the freely vibrating CML

is able to match the NEKTAR results. At higher values of $S_G$, however, the CML model grossly underpredicts the amplitude of vibration.

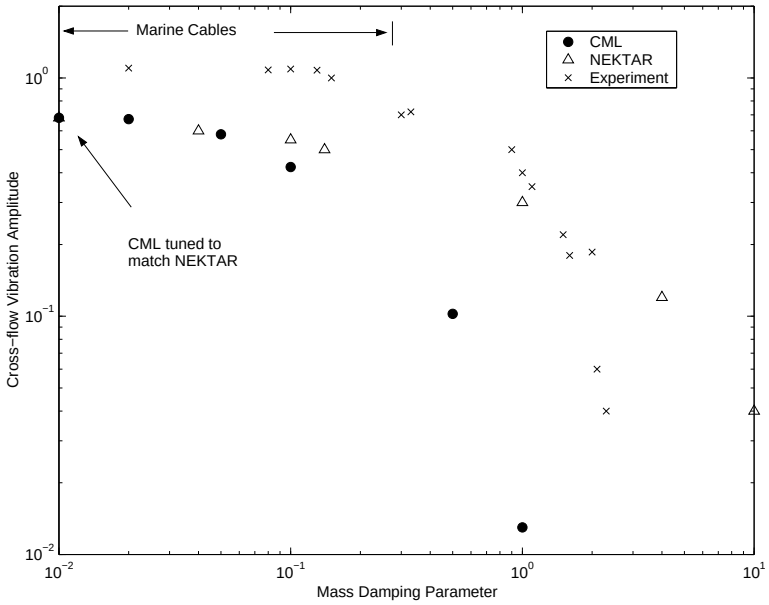


Figure 3.22: Vibration Amplitude vs. Mass-Damping Parameter (NEKTAR data taken from [14], experimental data taken from [7])

As in the earlier comparisons, the discrepancies in predicted amplitude values between the two models are attributed to the wake dynamics that are unmodeled in the CML This seems reasonable, since the dynamic model for the cable used in both the freely vibrating CML and the NEKTAR simulations is identical. By modeling more of the terms in the vorticity transport equation (Equation 2.5), or by utilizing a self-learning CML to adaptively update the values of $C_l$ and $G$, it is expected that the range of $S_G$ values over which the CML can match NEKTAR results would be extended. Addition of self-learning features to the CML model will be briefly addressed in a later section.

## 3.3 Experimental Setup and Data Acquisition

The purpose of this section is to describe in detail the experimental apparatus and techniques used in the collection of wake data. It was discussed in the introduction that experimental wake patterns were measured for two purposes: the first is for direct comparison with the wake patterns output from the freely vibrating CML model, and the second is to supply data to a self-learning CML algorithm. The wake data is collected through the use of hot-film anemometers placed in the cable wake to measure the streamwise velocity at several locations along the cable span simultaneously. A correlation algorithm was then developed in order to convert the velocity data gathered in the experiment to wake patterns that are analogous to the output of the CML.

## 3.4 Facilities and Setup

All experiments were conducted in the WPI free surface, re-circulating water tunnel. The tunnel has a reported turbulence level of below 1%. Prior to entering the test section of the tunnel, the flow is passed through honeycomb screens for flow straightening and accelerated through a 7:1 contraction. The tunnel test section is 2.4  long, with cross sectional dimensions of 60 by 60 $cm$. The water level in the test section was set at 64 $cm$, which was the level used at calibration.

A diagram of the setup in the tunnel test section can be seen in Figure 3.23. Through the use of suction cups, an aluminum plate was fastened to the bottom of the tunnel. This plate has a thin metal bar embedded in it that allows for a fastening hook. Thus, cables to be studied are fitted at the end with a fastening hook and hooked to the bottom plate. The cable is then run through a hole in a metal extension apparatus, which forms the pinned boundary condition just above

the water surface at the top of the tunnel. Once passing through this support, the cable is wrapped around a pulley that is used to adjust the tension of the cable.

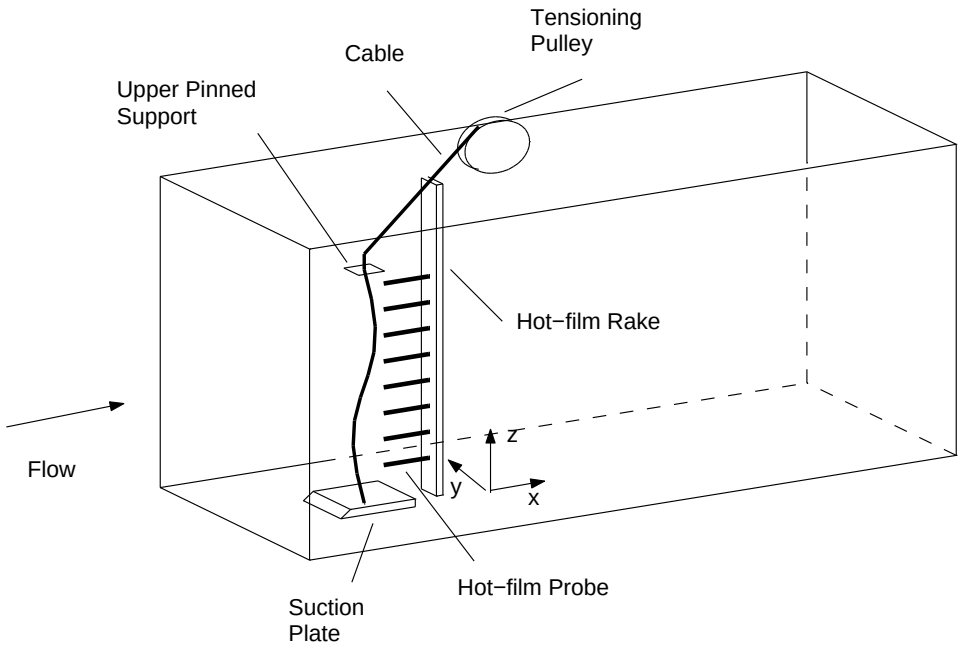


Figure 3.23: Diagram of Experimental Setup in Test Section of Water Tunnel

The coordinate system that is used in the experimental study is similar to that of the CML. The origin for the system will be located at the attachment point of the cable to the aluminum plate at the bottom of the tunnel. The $x$, $y$, and $z$ directions once again represent the streamwise, transverse, and spanwise directions, respectively.

All of the cable geometry and flow parameters used through out all experiments in this thesis are summarized in Table 3.3. The reported Reynolds number for the study is 260; this number is more than double the value of 100 used for the CML

studies. The higher experimental Reynolds number is a result of some practical limitations of the experiment. The free-stream velocity of 10 $cm/s$ is the lowest velocity the tunnel can operate at with out cavitation in the tunnel pump. Initially, smaller cable diameters were chosen so as to reduce the Reynolds number to 100. However, the smaller diameters made it increasingly difficult to make reliable velocity measurements in the cable wake. The chosen values of cable diameter and free stream velocity represent the smallest values that could be used in order to still obtain reliable wake data.

| Parameter | Value |
|---|---|
| Cable Length $L$ | 68 $cm$ |
| Cable Diameter $d$ | 0.3 $cm$ |
| $U_\infty$ | 10 $cm/s$ |
| $AR$ | 227 |
| $Re$ | 260 |
| $St$ | 0.195 |
| $f_{so}$ | 6.5 $Hz$ |

Table 3.3: Cable Geometry and Flow Parameters

A hot-film rake is placed in the wake of the cable. Eight hot-film anemometer probes are spaced along the cable span in order to measure the streamwise velocity component of the wake. The rake was displaced transversely off the cable centerline and angled in to the cable in order that the rake support apparatus disrupt the flow field as little as possible. The final locations of the hot-film probes in relation to the cable were set to be at a down stream distance of approximately $x/d = 7 - 10$. This was found to be the optimal range for the collection of velocity data. In addition, the probes were positioned transversely off the cable centerline by approximately one diameter, in order to try to isolate the data collection to a single shear layer. The locations of the eight probes along the cable span are presented in Table 3.4. The lower cable attachment is at $z/d = 0$, and the upper attachment is at $z/d = 227$.

Also included in the table are the locations of cable nodes and anti-nodes.

| Probe Number | $z/d$ Location |
|---|---|
| Node | 0 |
| 1 | 25.4 |
| 2 | 44.5 |
| Anti-node | 56.8 |
| 3 | 63.5 |
| 4 | 82.6 |
| 5 | 101.6 |
| Node | 113.5 |
| 6 | 120.7 |
| 7 | 138.7 |
| 8 | 158.8 |
| Anti-node | 170 |
| Node | 227 |

Table 3.4: $z/d$ Location of Hot-Film Probes and Cable Nodes and Anti-nodes

## 3.5 Instrumentation

The hot-film probes used in the acquisition of velocity data were TSI model 1020-W film sensors. The eight velocity probes are used in conjunction with a TSI IFA 300 Constant Temperature Anemometer System. A schematic diagram of the velocity data acquisition system is presented in Figure 3.24.

The IFA 300 cabinet contains the bridge and amplifier circuits needed to control the hot-film sensors. Output from the IFA 300 is an analog voltage proportional to fluid velocity, which is fed in to an United Electronic Industries WIN30 Analog to Digital data acquisition card, which has a maximum data throughput rate of 1 MHz. The A/D card is inserted into a PC running MS Windows 2000. All setup and data acquisition is accomplished through the use of the TSI ThermalPro software, version 2.20. Communication between the acquisition software and the anemometer

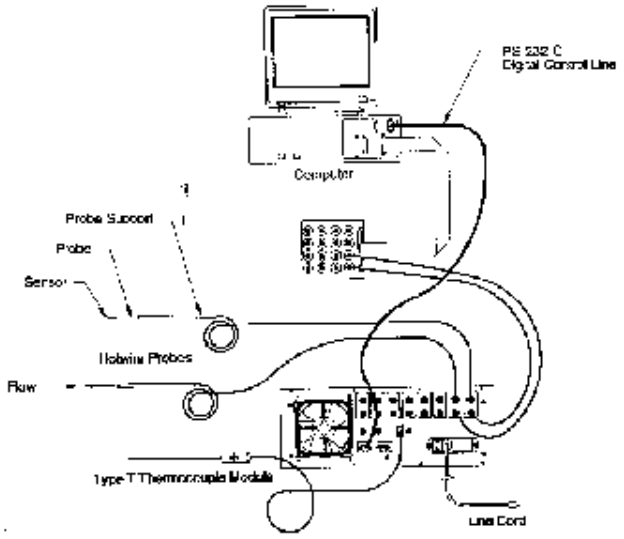


Figure 3.24: Overview of the IFA 300 Anemometer System

cabinet occurs via an RS-232-C digital control line.

## 3.6 Acquisition of Velocity Data

From Table 3.3, the stationary shedding frequency for the cable geometry used in this study is expected to be $f_{so} = 6.5\ Hz$. This value was calculated based on the Reynolds number from the Roshko empirical relation (Equation 1.2). In obtaining wake patterns from the velocity data, it will be necessary to extract the primary shedding frequency of the wake.

All velocity data that was collected was sampled at a rate of $f_s = 100\ Hz$. To avoid aliasing, a low-pass anti-aliasing filter with a cutoff frequency of $f_N = 50\ Hz$. Since the primary frequencies of interest will be at or near the Strouhal frequency,

this sampling rate provides more than enough bandwidth for the study.

## 3.7 Velocity Correlations

Once the velocity time histories of the eight hot-film probes are acquired, frequency domain correlation techniques is applied to the data in order to calculate wake patterns analogous to those computed by the CML. The algorithm used to accomplish this calculation will now be described.

As a first approximation, assume that the velocity traces at positions downstream of the cable can be represented as sine waves with a phase angle and amplitude that are functions of their $z$ $(k)$ location. That is,

$$u(z,t) = K(z)\sin(2\pi f_{so}t + \phi(z)). \tag{3.4}$$

Thus, in order to determine $\theta_n^k$, the phase angle must be extracted. To do this, a reference point is chosen and then correlations between the velocity history at each desired point and the baseline are needed. One potential method for determining these correlations and thus the phase angles between the velocity traces is to use frequency domain methods.

The correlation integral between two velocity time histories (call them $u_1$ and $u_2$) is defined to be

$$\int_{-\infty}^{\infty} u_1(\tau)u_2(t+\tau)d\tau. \tag{3.5}$$

The correlation integral and the Cross Power Spectrum form a Fourier Transform pair. That is, the Cross Spectrum is the Fourier Transform of the correlation integral,

$$\int_{-\infty}^{\infty} u_1(\tau)u_2(t+\tau)d\tau \Leftrightarrow G_{u_1u_2}, \tag{3.6}$$

where $G_{u_1u_2}$ is the Cross Power Spectrum and the double-headed arrow denotes transformation between the time and frequency domains.

The Cross Spectrum can be calculated from the Fourier Transforms of the individual time histories. Thus, if $U_1(f)$ and $U_2(f)$ are the Fourier transforms of $u_1(t)$ and $u_2(t)$ respectively, then the Cross Spectrum $G_{u_1u_2}$ is

$$G_{u_1u_2}(f) = U_1(f) \cdot U_2(f)^*. \tag{3.7}$$

The asterisk in the above equation denotes taking the complex conjugate. It should be noted that $G_{u_1u_2}(f)$ is a complex quantity. It can be placed in polar form (magnitude, angle) for the purposes of determining the phase difference between two signals.

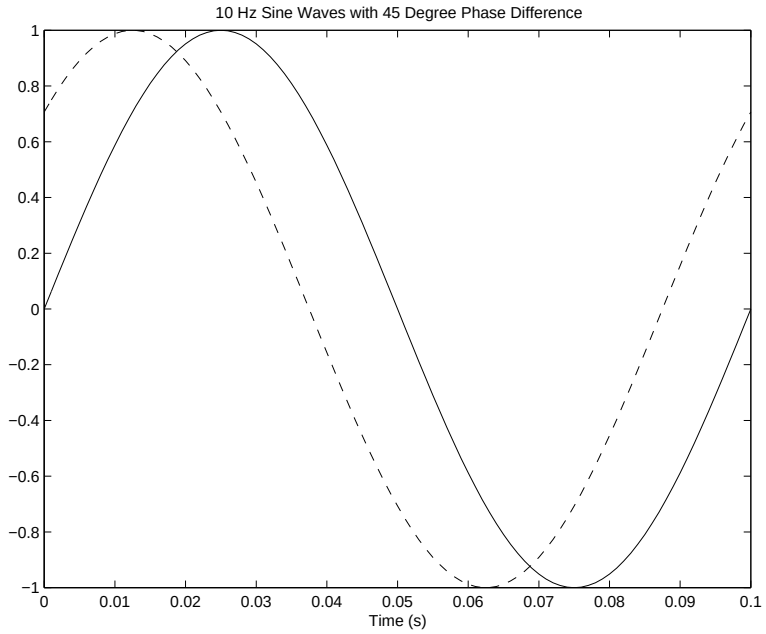


Figure 3.25: Time histories of sample signals

As a simple example, consider two $10Hz$ sine waves with a $45°$ phase difference. The time traces of the two signals can be seen in Figure 3.25.

By taking the Fourier transforms of both signals and then calculating the Cross Spectrum, the $45°$ phase difference can be observed. Figure 3.26 shows the magnitude and phase as a function of frequency for the cross spectrum of the two signals presented in Figure 3.25.

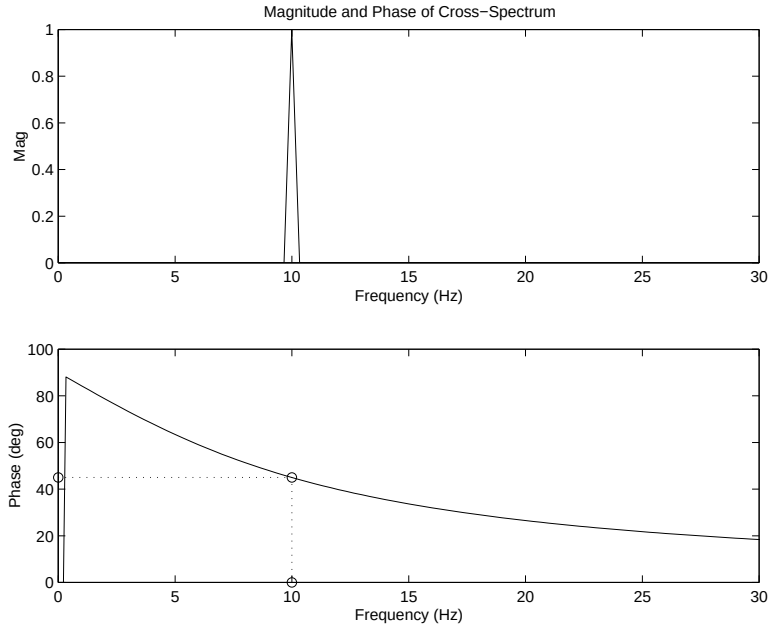


Figure 3.26: Bode Diagram for Cross Spectrum of sample signals

The magnitude portion of the Figure clearly shows that there is only one significant component to the signal, at $10Hz$. Moving to the phase diagram, it is easily verified that the $10Hz$ frequency component has a phase angle associated with it of $45°$.

Recall that $\theta_n^k$ is defined modulo one. Therefore, once the phase angle at a particular location is determined, is is normalized by $2\pi$ to give its corresponding $\theta$ value.

## 3.8 Experimental Results

In order to match as closely as possible the conditions of the CML studies, the cable tension is set so as to match the second harmonic of the natural frequency of the cable to the Strouhal frequency ($f_{so} = 6.5Hz$). This was accomplished using a MTI Photonic Sensor (which measures cable displacement) mounted above the free surface of the water; the cable tension is set and then the frequency of vibration determined by plucking the cable and examining the output of the MTI probe. The cable tension was adjusted such that the resulting cable vibration frequency was approximately 3.25 $Hz$, or half the natural shedding frequency of the cable. Again, this was done to tune the *second* harmonic to an $\Omega = 1$ lock-on condition, in order to be consistent with the CML studies. The presence of a second harmonic mode shape was confirmed visually with the help of a strobe light. The tunnel was run at the desired free stream velocity for the experiments ($U_\infty = 10\ cm/s$) to excite the cable, and by strobing the system a node near the cable mid-span was clearly visible. Assuming that the cable mode shape is a sine wave, the location of the nodes and anti-nodes of the cable were presented above in Table 3.4

A sample velocity time history taken from the cable wake is presented in Figure 3.27. This is the raw velocity data from probe number one, which is located 3 $in$ from the bottom of the tunnel test section, at a $z/d$ location of $z/d = 25.4$, roughly halfway between a node and an anti-node. Note that even at low Reynolds number ($Re = 260$) the velocity time history is quite complex. Also included are the velocity time histories for probes three and six in Figures 3.29 and 3.30. Probe three is located near a cable node, and probe six is near a cable anti-node. Note the differences in mean velocity and amplitude fluctuation.

After subtracting out the mean velocity component, the magnitude of the fre-

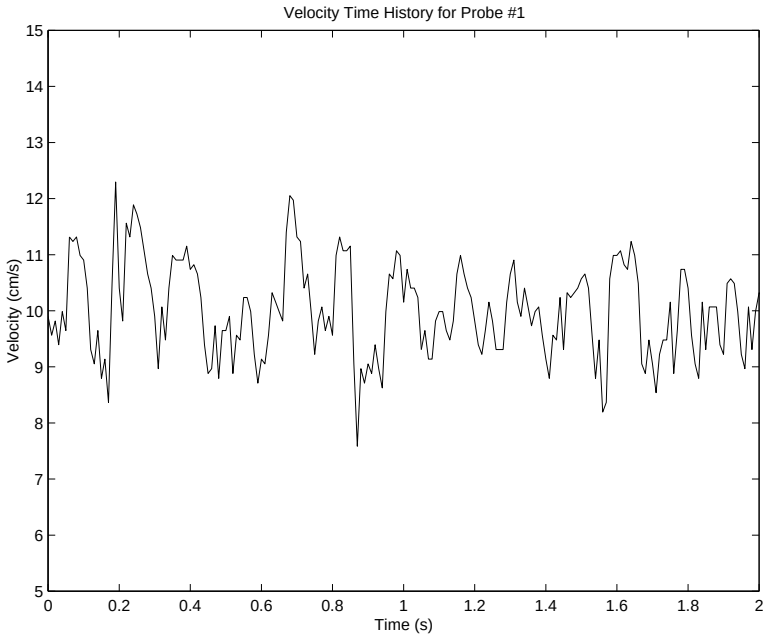


Figure 3.27: Velocity Time History of Probe 1

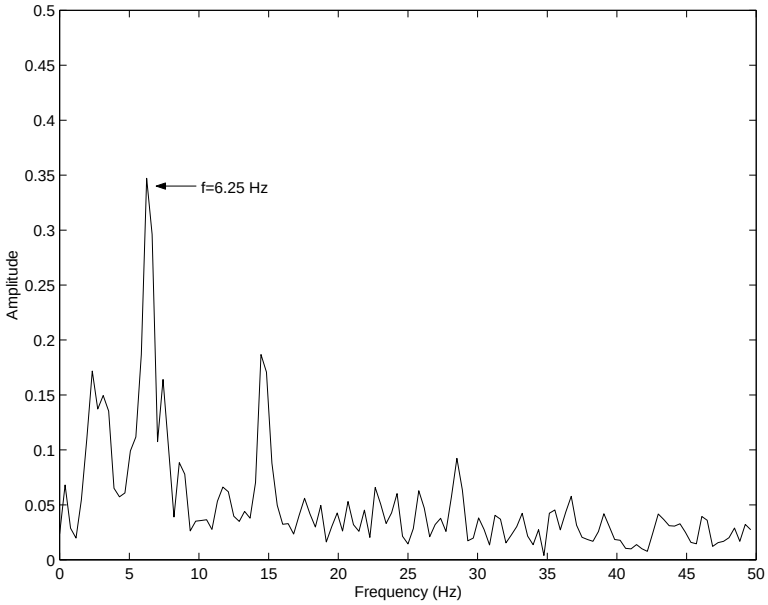


Figure 3.28: Frequency Spectrum of Velocity, Probe 1

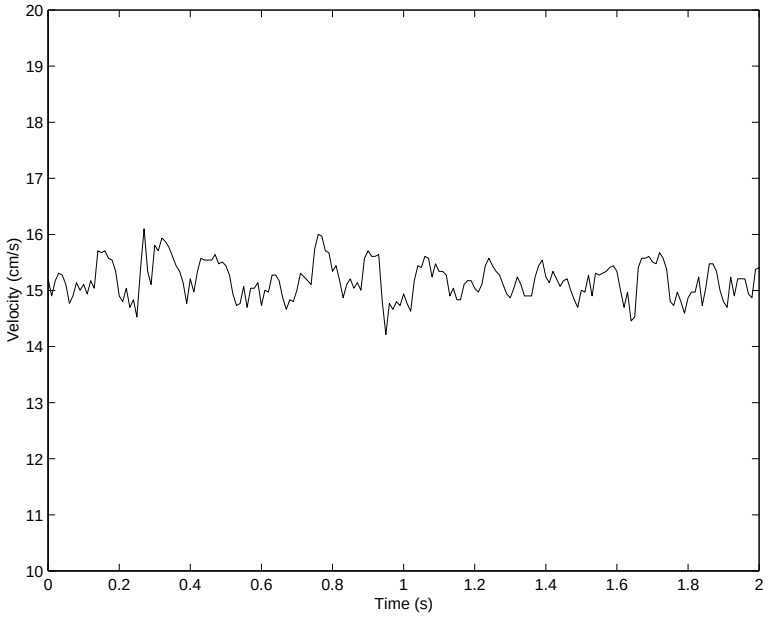


Figure 3.29: Velocity Time History of Probe 3

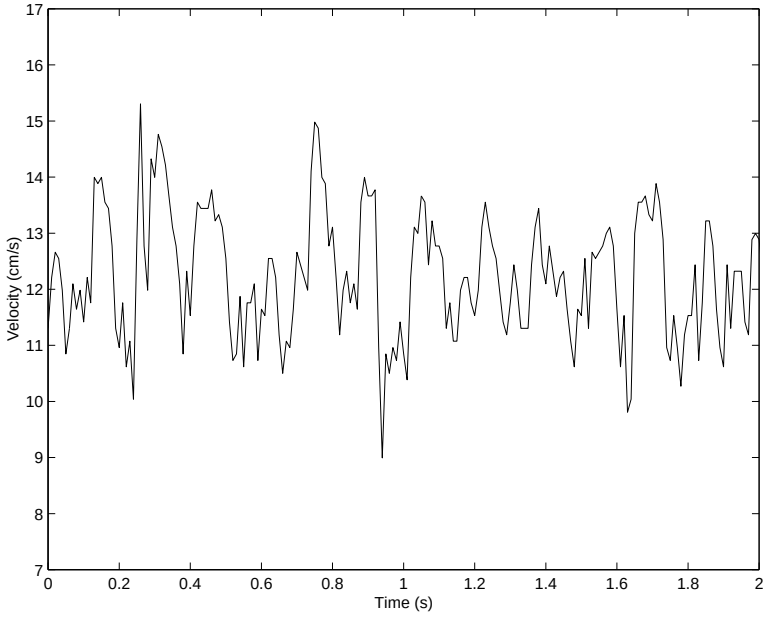


Figure 3.30: Velocity Time History of Probe 6

quency spectrum of the time history of Figure 3.27 is presented in Figure 3.28. Since the time domain plot is fairly complex, it is not surprising to see significant amplitudes across a wide range of frequencies. There is, however, a clear, distinct peak located at a frequency of $f = 6.25\ Hz$. This value is extremely close to the calculated stationary shedding frequency of $f_{so} = 6.5\ Hz$. This frequency will be used in the velocity correlation algorithm as the dominant shedding frequency in the wake for the purposes of calculating wake patterns.

The procedure for calculating the resulting wake pattern for this particular data set will be outlined by demonstrating the calculation of the phase angle between probes one and two. Probe one is taken to be the reference point for all phase calculations; consequentially, the value of $\theta$ at the location of probe one will be identically zero.

As described in Section 3.7, the cross power spectrum of the velocity time histories between probes one and two is calculated. The magnitude and phase of this cross power spectrum are presented in Figures 3.31 and 3.32.

Examining the magnitude portion of the cross power spectrum, the large peak near the cylinder shedding frequency is clearly evident. The phase angles have been normalized by $2\pi$ in order to make them consistent with the modulo one representation of $\theta$. In order to determine the value of $\theta$ at the second probe location, the $\theta$ value at the dominant shedding frequency of $f = 6.25\ Hz$ is read off of the phase plot. Following this procedure, cross correlations between probes two through seven and probe one are calculated, and the resulting phase angle at the appropriate frequency is recorded. This algorithm provides the distribution of $\theta$ along the span of the cable. The resulting experimental wake pattern is presented in Figure 3.33.

The arrows on the figure indicate the locations of cable nodes and anti-nodes. Also included in Figure 3.33 is a similar result from NEKTAR. In earlier comparisons

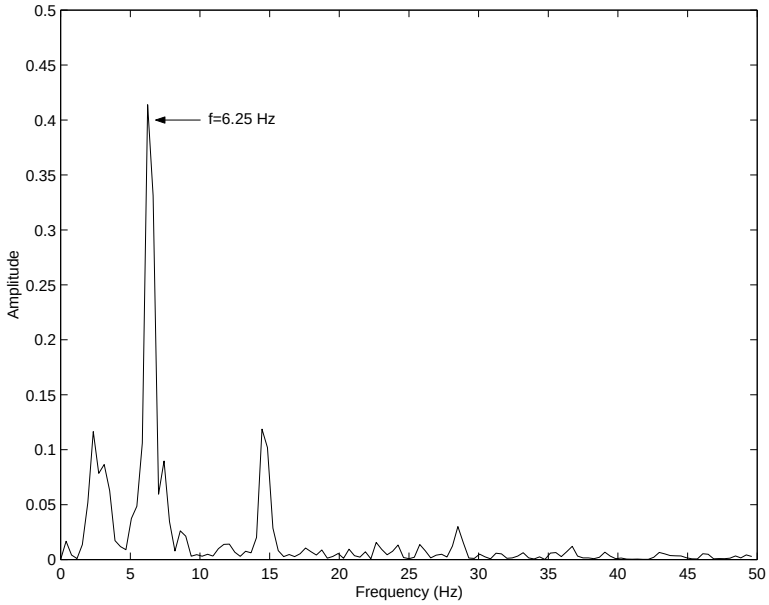


Figure 3.31: Magnitude of Cross Correlation Between Probes 1 and 2

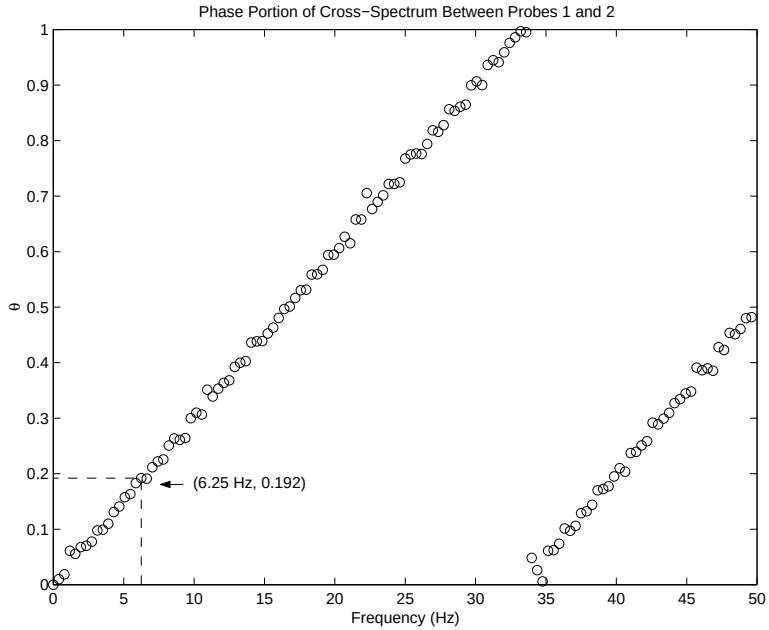


Figure 3.32: Phase of Cross Correlation Between Probes 1 and 2

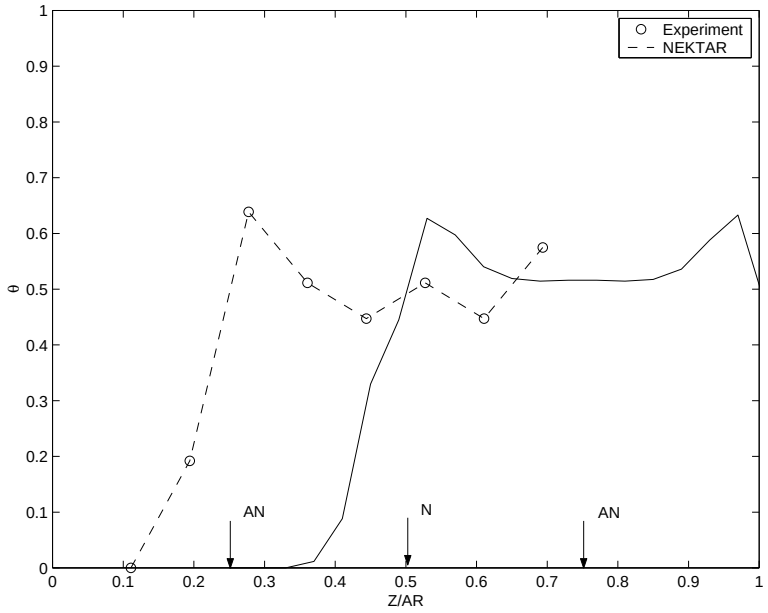


Figure 3.33: Experimental Wake Pattern

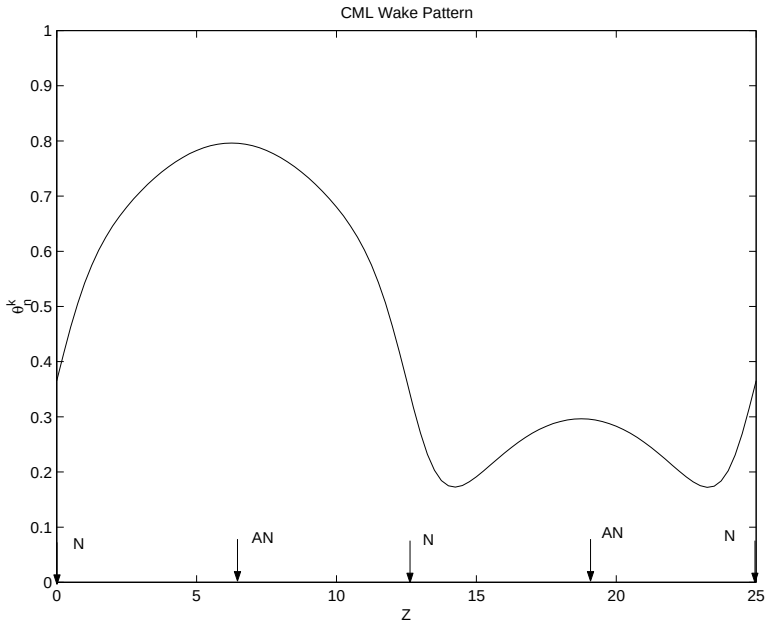


Figure 3.34: $\theta$ (CML) Distribution of Single Shear Layer for Comparison with Experiment

with NEKTAR, wake patterns were visualized through contour plots of streamwise vorticity. Using the hot-film probe rake, it is not possible to produce similar vorticity contours for comparison. NEKTAR, however, is capable of providing streamwise velocity data. The velocity correlation algorithm is then applied to this NEKTAR data, and the NEKTAR analog to the experimental wake pattern is produced. Finally, a wake pattern output from the freely vibrating CML is presented in Figure 3.34.

The experimental and NEKTAR results show very similar wake patterns, with a spanwise shift between the two. The experimental pattern shows a peak near a cable anti-node, while the corresponding peak in the NEKTAR pattern is centered about a cable node. A couple of explanations are offered for this spanwise shift; first, the aspect ratios of the two results are drastically different (227 for the experiment, $4\pi$ for NEKTAR), and there are different end conditions. The boundary conditions on the NEKTAR results are periodic out to infinity, while there are obviously physical boundaries in the water tunnel. Comparisons with the CML results show less agreement. Still, both patterns might qualitatively be described as lace-like, and both show $\theta$ peaks near anti-nodes. Also, while the CML wake patterns are calculated at $k^* = 101$ spanwise locations, only 8 velocity probes are available in the experiment.

It is important to emphasize that the resulting wake pattern obtained is an *average* pattern. That is, it is the average phase angle distribution over several shedding cycles. The time record length of the velocity data is 2.04 $s$. At the shedding frequency of $f = 6.25\ Hz$, their are slightly more than twelve shedding cycles occurring over this length of time. Eventually it is desired to calculated wake patterns for *each* shedding cycle. However, due to the complexity of the velocity data this is an extremely difficult task to do. The current correlation algorithm depends heavily that the time domain data be strongly periodic. Thus, several

seconds of velocity data are necessary. Higher order correlation algorithms [2] that focus on complex filtering techniques may hold the key to solving this dilemma. Experiments at lower Reynolds number (to match CML models) where the wake is more ordered are also desirable, but difficult to achieve in the WPI water tunnel due to the facility limitations mentioned earlier.

## 3.9 Self-Learning CML

It has been often mentioned throughout this thesis that the potential remedy for some of the shortcomings of the freely vibrating CML is the inclusion of a self-learning capability to the model. Using the freely vibrating CML as its core, this self-learning CML would be able to utilize wake data from an experiment (or from CFD studies) to capture those dynamics that the CML is unable to model.

In order to demonstrate that this approach has potential, the experimental wake data presented above was used in the self-learning *forced* CML model of Balasubramanian, et. al. [3] [4]. The CML model from which this self-learning scheme is based does not include the cable dynamics in the form of the wave equation used in this study. It does, however, retain additional terms in the vorticity transport equation (Equation 2.5), as well as the self-learning capability. A schematic diagram of how such a system works is presented in Figure 3.35.

Using the correlation routines, target states $X_n^k$ (which are simply experimental $\theta_n^k$ values are compared with the estimated target states output from the self-learning adaptive CML, generating a state error term. The adaptive estimation scheme then seeks to drive this state error to zero, and over time, the CML model is able to predict the target states.

A brief summary of this self-learning algorithm will be presented below. For a

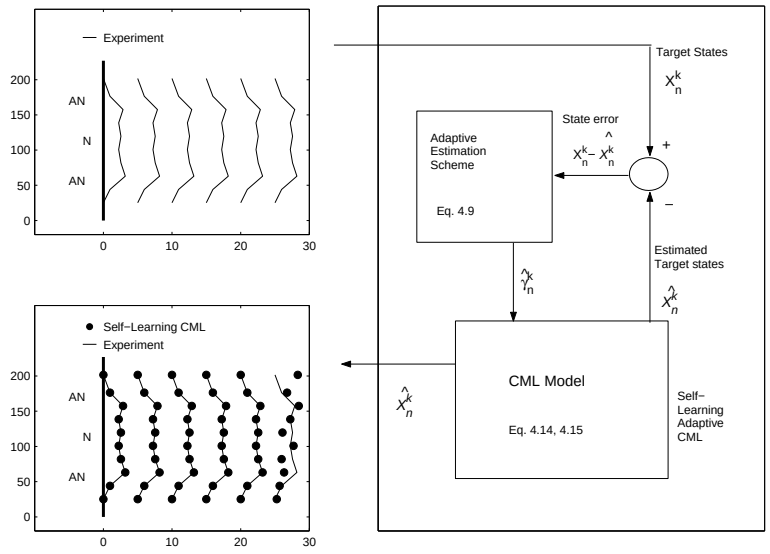


Figure 3.35: Schematic of Self-Learning CML Model

detailed discussion of the self-learning CML, the reader is directed to the results presented in [3], [4].

As mentioned, the self-learning scheme utilizes a new convective-diffusive CML,

$$\begin{aligned} X_{n+1}^k &= [\epsilon f_n^{k-1} + (1-2\epsilon) f_n^k + \epsilon f_n^{k+1}] + \\ &\quad \frac{1}{2}[-f_n^k \gamma^{k-1} + (f_n^{k-1} - f_n^{k+1}\gamma^k + f_n^k \gamma^{k+1}], \qquad (3.8) \\ f_n^k &= X_n^k + \Omega^k - \frac{K^k}{2\pi} \sin\left[2\pi X_n^k - \phi_1^k - \frac{\pi}{2}\right]. \qquad (3.9) \end{aligned}$$

The first term in Equation 3.8is the familiar diffusive coupling between oscillators; the second is a new convection term, where $\gamma^k = w^k \Delta t / \Delta z$. The term $w^k$ is the spanwise convection velocity and is a new term in the map, and $X_n^k$ replaces $\theta_n^k$ as the phase of vortex shedding.

Equation 3.8 can be written in matrix from as

$$X_{n+1} = A(\epsilon)F(X_n) + G(X_n)\Gamma \tag{3.10}$$

$$= A(\epsilon)F(X_n) + Y_n \tag{3.11}$$

In Equation 3.11, $\Gamma = [\gamma^1, \gamma^2, ..., \gamma^{k^*}]$ is the vector of spanwise velocities at the oscillator locations. The adaptive CML is modeled as

$$\hat{X}_{n+1} = A(\epsilon)F(X_n) + G(X_n)\hat{\Gamma}_n, \tag{3.12}$$

$$= A(\epsilon)F(X_n) + \hat{Y}_{n+1}, \tag{3.13}$$

where $\hat{X}$ is the estimate of the state variable $X$ and $\hat{\Gamma}$ is the estimate of the spanwise velocity. The state error is defined as

$$e_{n+1} = \hat{X}_{n+1} - X_{n+1}, \tag{3.14}$$

$$= \hat{Y}_{n+1} - Y_{n+1}, \tag{3.15}$$

$$= G(X_n)\hat{\Gamma}_n - Y_{n+1}. \tag{3.16}$$

It is desired to drive the state error to rest in the shortest possible time. In order to accomplish this, a multivariable least-squares algorithm is used to minimize the state error after each time step [5]:

$$J_N(\hat{\Gamma}_{n+1}) = \frac{1}{2}(\hat{\Gamma}_{n+1} - \hat{\Gamma}_0)^T P_0^{-1}(\hat{\Gamma}_{n+1} - \hat{\Gamma}_0) +$$

$$\frac{1}{2}\sum_{n=1}^{N}(Y_{n+1}-G(X_n)\hat{\Gamma}_{n+1})^T R^{-1}(Y_{n+1}-G(X_n)\hat{\Gamma}_{n+1}). \quad (3.17)$$

The first term in Equation 3.17 accounts for errors in initial parameter estimates and the second term represents the weighted sum of the squared state errors. Minimizing Equation 3.17 with respect to $\hat{\Gamma}_{n+1}$,

$$P_n = P_{n-1} - P_{n-1}G(X_n)^T(R+G(X_n)P_{n-1}G(X_n)^T)^{-1}G(X_n)P_{n-1}, \quad (3.18)$$

$$\hat{\Gamma}_{n+1} = \hat{\Gamma}_n - P_n G(X_n)^T R^{-1} e_{n+1}. \quad (3.19)$$

Equation 3.19 is the update law for $\hat{\Gamma}_{n+1}$, with the covariance matrix $P_n$ defined as:

$$P_n^{-1} = \left(P_0^{-1} + \sum_{n=1}^{n} G(X_i)^T R^{-1} G(X_i)\right). \quad (3.20)$$

Equations 3.18, 3.19 along with Equation 3.13 form the proposed self-learning CML.

Using these methods, the experimental wake pattern of Figure 3.33 was estimated by the self-learning CML. The results are presented in Figure 3.36.

In order to perform the estimation, false mirror points were added to the experimental wake pattern to create a symmetric $\theta$ distribution along the span. The total number of circle map oscillators used was $k^* = 10$. The estimator model is able to match the experimental wake identically. Again, in the future, it is desired that a wake pattern for *each* shedding cycle (rather than an average wake pattern over several shedding cycles) be input to the self-learning model.

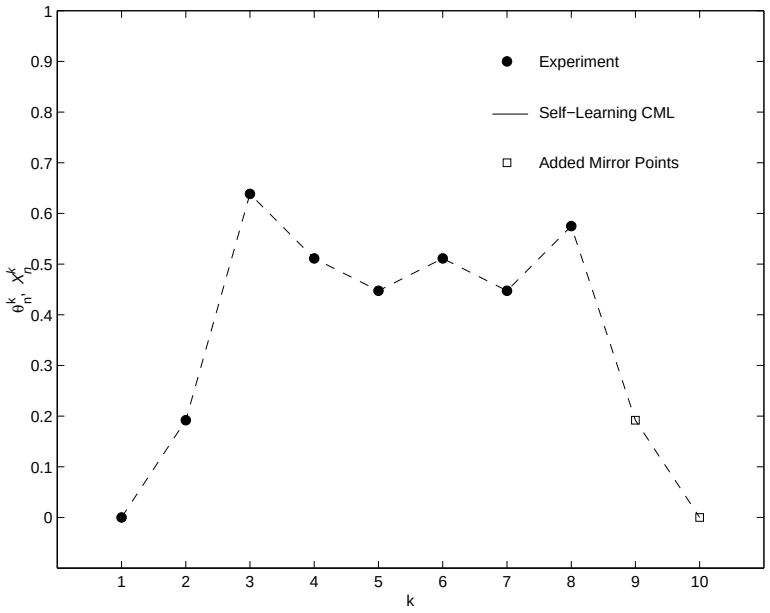


Figure 3.36: Estimation of Experimental Wake Pattern by Self-Learning CML

# Chapter 4

# Conclusions and Summary

This thesis has sought to model the problem of the self-induced vibration of a flexible cable at low Reynolds number through the use of low order dynamic models. Through the coupling of a Coupled Map Lattice wake model with a linear wave equation, both the response of the cable and the structure of the cable wake were predicted. In order to assess the validity of the model, comparisons were made with the CFD simulations of Newman and Karniadakis [14] [15]. Furthermore, a wake experiment was devised to provide experimental wake patterns that could also be compared with the output of the freely vibrating CML model.

The low-order approach to modeling the freely vibrating cable wake depends heavily on knowledge gained from previous experiments and numerical simulations on wake flows. Input parameters such as the Strouhal frequency of vortex shedding [20], vortex convection velocity [26], and the phase angles [18] (between the vortex shedding event and either cylinder motion or lift force as a function of cable amplitude) are all obtained from previous wake studies. The main advantage of the low-order approach is its computational efficiency; the freely vibrating CML requires $10^4$ fewer wall clock seconds per shedding cycle in its execution than does

the NEKTAR simulations.

The first problem that was examined was the case of the self-excited response of an elastically mounted rigid cylinder. Using a modified sine circle map as the wake model, the resulting cylinder motion was determined by coupling the wake model with a mass-spring-damper dynamic system. Prior to utilizing the model in full, a parametric study was conducted in order to determine the proper level for the free parameters $C_l$ and $G$. The final values of the free parameters were chosen such that the amplitude of vibration matched the NEKTAR predictions under similar flow conditions and cylinder geometry.

Once the free parameters were found, the natural frequency of the cylinder was tuned to match its shedding frequency, in order to study the 1/1 ($\Omega = 1$) lock-on condition. The two-dimensional model was then iterated until both the wake and cylinder motion achieved a steady-state, time periodic response. Output from the model were the amplitude and frequency of the cylinder motion and the shedding frequency of the wake.

The frequency ratio $\Omega$ was then varied to examine other lock-on cases. It was found that the maximum amplitude of vibration occurred at a frequency ratio of $\Omega = 1.1$. The occurrence of the peak amplitude at a frequency ratio other than $\Omega = 1$ is characteristic of a self-induced oscillator. In comparing these results with NEKTAR simulations, it was found that while the general trends and the magnitude of the maximum vibration amplitude were consistent, the frequency at which this maximum occurred was shifted significantly with respect to the NEKTAR results. The frequency of cylinder vibration was seen to vary in a linear manner with $\Omega$ across the entire range. NEKTAR results showed similar behavior near $\Omega = 1$, but outside of this narrow band of frequency ratio the two models failed to correlate well at all.

Using some of the insight gained from the two-dimensional simulations, the flexible cable problem was examined in detail. Specifically, the problem studied was that of a second mode standing wave cable response. This condition was chosen so as to be as consistent as possible with both the NEKTAR and experimental results. After the tuning of the free parameters $C_l$ and $G$ in a manner analogous to that described above for the 2-D case, the second natural frequency of the cable was set to match the natural shedding frequency of the cable. Random initial conditions were employed on both the cable amplitude and wake. The resulting cable motions and wake patterns were then iterated to steady-state values, giving answers that were independent of initial conditions.

Once again, the first case studied was that of a 1/1 lock-on condition. The cable was found to vibrate in a second mode standing wave pattern at the shedding frequency of the cable. The wake patterns were found to be interwoven in a lace-like fashion, with a distinctive "M" shaped profile centered around cable anti-nodes. Qualitatively, these results matched well with the NEKTAR studies. Furthermore, comparisons between results gathered from the freely vibrating CML and the externally forced CML (free vibration versus forced vibration) showed little to no differences, which was consistent with a similar NEKTAR study at the same Reynolds number. An additional study at 1/1 resonance conditions involved the varying of the mass-damping parameter $S_G$; it was found that the freely vibrating CML was capable of matching numerical results of maximum amplitudes of vibrations over an order of magnitude in $S_G$, once the model was tuned to match the numerical study at $S_G = 0.01$. The range over which the two models show good agreement is the range of $S_G$ typically reported for marine-type cables.

Studies of off-resonance cases ($\Omega = 0.99$) showed that the cable once again vibrated in a second mode standing wave condition, although the mode shape observed

was slightly asymmetric. The wake pattern showed vortex dislocations present near cable nodes. It was speculated that this was a result of different lock-on conditions existing along the cable span, with the wake near cable anti-nodes remaining in a 1/1 lock-on state, while the wake at lower vibration amplitudes moving in to more complicated lock-on conditions. These dislocations in the wake then contributed to the asymmetric cable vibration.

Finally, experimental wake patterns were obtained through hot-film velocity measurements at different locations along the cable span. A correlation algorithm was developed based on the cross-power spectrum in order to determine the phase differences between the velocity time histories. The variation of phase lag along the cable span provided a crude estimate of the wake pattern behind the cable.

Comparisons between the CML and the experimental results were difficult to perform; with only eight hot-film probes, the experimental wake pattern was rather sparse. However, both results provided wake patterns that could qualitatively be deemed lace-like, and both showed an "M" shaped profile within the pattern. The location of this characteristic "M" shape was not consistent between studies; CML results showed the "M" being centered around cable anti-nodes, while the experiments predicted its presence near nodes.

This thesis has successfully shown that certain aspects of the wake behind a freely vibrating cable can be modeled using coupled map lattices. The ability of the freely vibrating CML to match other results is most promising in 1/1 resonance conditions (the $\Omega = 1$ case). It is hoped that this freely vibrating CML model can serve as the core of a self-learning freely vibrating CML, that would be better equipped to model the more complex dynamics that occur in off-resonance cases. Aside from incorporating self-learning features, other ways of coupling the CML to the wave equation could be examined. Skop and Balasubramanian [21] suggest the

inclusion of a stall term in the cable forcing (Equation 2.91 for the freely vibrating CML) to ensure that the magnitude of the fluctuating lift force has a negative slope for large amplitude cylinder motions, a result that has been observed in experiments [23].

In addition, further work could also focus on refining the experiment to measure wake patterns. Obtaining measurements at lower Reynolds number, as well as including more velocity probes, would assist in obtaining more meaningful wake patterns. New correlation routines would also be useful in this regard, due to the complex nature of the experimental velocity time histories. Eventually the acquisition of one wake pattern per shedding cycle is desired, and the improvement of the data acquisition and correlation routines is most likely the fastest way to accomplish this.

# Bibliography


[1] P. W. Bearman. Vortex shedding from bluff bodies. *Annual Review of Fluid Mechanics*, Vol. 16, 1984.

[2] P. Bloomfield. *Fourier Analysis of Time Series*. John Wiley and Sons, 1976.

[3] M. A. Demetriou G. Balasubramanian, D. J. Olinger and M. P. Davis. Development of a self-learning scheme for modeling cylinder wakes behind flexible cables. *Journal of Fluids and Structures (submitted)*, 2001.

[4] M. A. Demetriou G. Balasubramanian, D. J. Olinger and M. P. Davis. Development of a self-learning coupled map lattice scheme for modeling cylinder wakes. *2001 Fluids engineering division's summer meeting forum on unsteady flows*, 2001.

[5] G. C. Goodwin and K. S. Sin. *Adaptive Filtering, Prediction and Control*. Englewood Cliffs, NJ: Prentice Hall, 1984.

[6] Michael D. Greenberg. *Advanced Engineering Mathematics*. Prentice Hall, 1998.

[7] O. M. Griffin. Vortex-induced vibrations of marine structures in uniform and sheared currents. *NSF Workshop on Riser Dynamics, University of Michigan*, 1992.

[8] Klaus A. Hoffman. *Computational Fluid Dynamics for Engineers*. Engineering Education System, 1989.

[9] Mogens Hogh Jensen. Transition to chaos by interaction of resonances in dissipative systems. *Physical Review A*, Vol. 30, 1984.

[10] G. H. Koopman. The vortex wakes of vibrating cylinders at low reynolds numbers. *Journal of Fluid Mechanics*, Vol. 28, 1967.

[11] E. N. Lorenz. Deterministic nonperiodic flow. *Journal of the Atmospheric Sciences*, Vol. 20, 1963.

[12] Lefei Meng. Flow visualization of vortex shedding from a freely vibrating cable. Master's thesis, Worcester Polytechnic Institute, August 1996.

[13] P. A. Monkewitz. Phase Dynamics of Karman Vortices in Cylinder Wakes. *Physics of Fluids*, Vol. 8, 1996.

[14] D. Newman and G. E. Karniadakis. Simulations of flow over a flexible cable: a comparison of forced and flow-induced vibration. *Journal of Fluids and Structures*, Vol. 10, 1996.

[15] David J. Newman and G. Karniadakis. A direct numerical simulation of flow past a freely vibrating cable. *Journal of Fluid Mechanics*, Vol. 344, 1997.

[16] D. J. Olinger. *Universality in the transition to chaos in open fluid flows*. PhD thesis, Yale University, 1990.

[17] D. J. Olinger. A low-dimensional model for chaos in open fluid flows. *Physics of Fluids A*, Vol. 5, 1993.

[18] D. J. Olinger. A low-order model of vortex shedding patterns behind vibrating flexible cables. *Physics of Fluids*, Vol. 10, 1998.

[19] M. Provensal. Bernard-von karman instability: transient and forced regimes. *Journal of Fluid Mechanics*, Vol. 182, 1987.

[20] A. Roshko. On the development of turbulent wakes from vortex street. *NACA Report 1191*, 1954.

[21] R. A. Skop and S. Balasubramanian. A new twist on an old model for vortex-excited vibrations. *Journal of Fluids and Structures*, Vol. 11, 1997.

[22] R. A. Skop and O. M. Griffin. A model for the vortex-excited resonant response of bluff cylinders. *Journal of Sound and Vibration*, Vol. 27, 1973.

[23] M. S. Triantafyllou. Vortex-induced vibrations in a sheared flow: a new predictive method. *Hydroelasticity in Marine Technology*, 1994.

[24] D. J. Tritton. Experiments on the flow past a circular cylinder at low reynolds number. *Journal of Fluid Mechanics*, Vol. 6, 1959.

[25] T. von Karman. Uber den mechanisms des widerstandes, den ein bewegter korper en einer flussikeit erzeugt. *Nacht. Wiss. Ges. Gottingen. Math Phys.*, 1912.

[26] C. H. K. Williamson. Oblique and parallel modes of vortex shedding in the wake of a circular cylinder at low reynolds number. *Journal of Fluid Mechanics*, Vol. 206, 1989.

# Appendix A

# MATLAB Source Codes

## A.1 2-D Freely Vibrating CML

```
%%%%%%%%%%%%%%%%%%%%%%%%%%%%%%%%%%%%%%%%%%%%%%%%%%%%%%%%%%%%%%%%%%%%%%%%
%
% Fully Coupled 2-D Circle Map
%
%%%%%%%%%%%%%%%%%%%%%%%%%%%%%%%%%%%%%%%%%%%%%%%%%%%%%%%%%%%%%%%%%%%%%%%%

%%%%%%%%%%%%%%%%%%%%%%%%%%%%%%%%%%%%%%%%%%%%%%%%%%%%%%%%%%%%%%%%%%%%%%%%
%
% Initial Setup of Circle Map Input Parameters
%
%%%%%%%%%%%%%%%%%%%%%%%%%%%%%%%%%%%%%%%%%%%%%%%%%%%%%%%%%%%%%%%%%%%%%%%%
clear
ntime=200;
xko=0.05; admax=0.68;
slope=111; xinter=100;
slope2=-196; xinter2=50;
re=100; omega=1.5;
St=0.212-4.5/re;
theta_0=0.567;
pi=3.141592635;
Cl=1.04; rho=2;
Ko=0.4;
omega_n=2*pi/omega; zeta=0.01;

% Setup of System Matrices

A=[0 1; -omega_n^2 -2*zeta*omega_n];
```

```
B=[0 1]';
C=[1 0];
D=0;
sys=ss(A,B,C,D);

% Initial Conditions on Cylinder

y0=[0.01 0];
nsteps=10;     % number of sub-iterations
time=linspace(0,omega,nsteps+1);
f=zeros(length(time),1);

% Initial Phase Setup

aoverd=abs(y0(1))/xko*admax;
phase1=(slope2*aoverd+xinter2)*pi/180;
phase2=phase1;
phi1=(slope*aoverd+xinter)*pi/180;
phi2=phi1+pi;

theta=theta_0;
theta2=.786;
theta_n=theta+1;
theta_n2=theta2+1;

th=linspace(theta, theta_n, nsteps+1);
th2=linspace(theta2, theta_n2, nsteps+1);

%%%%%%%%%%%%%%%%%%%%%%%%%%%%%%%%%%%%%%%%%%%%%%%%%%%%%%%%%%%%%%%%%%%%%%%
%
% Start of Main Time Iteration Loop
%
%%%%%%%%%%%%%%%%%%%%%%%%%%%%%%%%%%%%%%%%%%%%%%%%%%%%%%%%%%%%%%%%%%%%%%%

for n=1:ntime

   %%%%%%%%%%%%%%%%%%%%%%%%%%%%%%%%%%%%%%%%%%%%%%%%%%%%%%%%%%%%%%%%%%%%%%%
   %
   % Integration of Cylinder Dynamics
   %
   %%%%%%%%%%%%%%%%%%%%%%%%%%%%%%%%%%%%%%%%%%%%%%%%%%%%%%%%%%%%%%%%%%%%%%%

   for l=1:nsteps
```

```
      f=2*Cl/(pi*rho)*(sin(2*pi*th-phase1)-...
sin(2*pi*th2-phase2));
      force(l+(n-1)*(nsteps))=f(l);
   end

   [y,t,x]=lsim(sys,f',time,y0);

   y0=x(nsteps+1,:);
   yout((n-1)*nsteps+1:n*nsteps+1)=y(1:nsteps+1);
   tout((n-1)*nsteps+1:n*nsteps+1)=t(1:nsteps+1)+(n-1);

   aoverd=abs(y(nsteps+1))/xko*admax;
phase1=(slope2*aoverd+xinter2)*pi/180;
phase2=phase1;
phi1=(slope*aoverd+xinter)*pi/180;
phi2=phi1+pi;


   theta=theta_n;
   theta2=theta_n2;
   %%%%%%%%%%%%%%%%%%%%%%%%%%%%%%%%%%%%%%%%%%%%%%%%%%%%%%%%%%%%
   %
   % Calculation of First and Second Shear Layers
   %
   %%%%%%%%%%%%%%%%%%%%%%%%%%%%%%%%%%%%%%%%%%%%%%%%%%%%%%%%%%%%

   ymax=max(y);
  ym(n)=ymax;

   theta_n=theta+omega-...
   Ko*ymax/(2*pi)*sin(2*pi*theta-phi1-.5*pi);
   theta_n2=theta2+omega-...
   Ko*ymax/(2*pi)*sin(2*pi*theta2-phi2-.5*pi);

   out(n)=mod(theta,1);
   out2(n)=mod(theta2,1);

end
```

## A.2 3-D Freely Vibrating CML

```
%%%%%%%%%%%%%%%%%%%%%%%%%%%%%%%%%%%%%%%%%%%%%%%%%%%%%%%%%%%%%%%%%%%%%%%%%%%%
%
% Fully coupled 3-D CML with wave equation
%
%%%%%%%%%%%%%%%%%%%%%%%%%%%%%%%%%%%%%%%%%%%%%%%%%%%%%%%%%%%%%%%%%%%%%%%%%%%%

%%%%%%%%%%%%%%%%%%%%%%%%%%%%%%%%%%%%%%%%%%%%%%%%%%%%%%%%%%%%%%%%%%%%%%%%%%%%
%
% Initial setup of CML input parameters
%
%%%%%%%%%%%%%%%%%%%%%%%%%%%%%%%%%%%%%%%%%%%%%%%%%%%%%%%%%%%%%%%%%%%%%%%%%%%%
clear
nz=101; ntime=400;          % Number of nodes, number of time steps
xko=0.05; xnwavef=100;     % Standing wavew amplitude, travelling wave length
admax=0.68;
slope=111; xinter=100;
slope2=-196; xinter2=50;
ar=25; re=100; ucu0=0.88;
eps=zeros(1,nz);    %diffusion coefficient
theta=zeros(nz,1);  %phase of shedding
theta2=zeros(nz,1);
thetan=zeros(nz,1);  %phase of shedding
thetan2=zeros(nz,1);
th=zeros(nz,1);
th2=zeros(nz,1);
pi=3.141592635;
st=0.212-4.5/re;    %strouhal relation
rho=2;
Cl=0.0001;
Ko=1.0;

b=0.05;
%%%%%%%%%%%%%%%%%%%%%%%%%%%%%%%%%%%%%%%%%%%%%%%%%%%%%%%%%%%%%%%%%%%%%%%%%%%%
%
% Initial Conditions for CML
%
%%%%%%%%%%%%%%%%%%%%%%%%%%%%%%%%%%%%%%%%%%%%%%%%%%%%%%%%%%%%%%%%%%%%%%%%%%%%

for k=1:nz
   omega(k)=0.95;
```

```
   eps(k)=omega(k)*(nz-1)^2/st/re/ar/ar/2/pi;
   theta(k)=abs(rand(1));
   theta2(k)=abs(rand(1));
   %theta(k)=0.999;
   %theta2(k)=0.999;
   Bmat(k)=theta(k);
   Bmat2(k)=theta2(k);
end

thetan=theta;
thetan2=theta2;
Amat=eye(nz);    % left hand side


%%%%%%%%%%%%%%%%%%%%%%%%%%%%%%%%%%%%%%%%%%%%%%%%%%%%%%%%%%%%%%%%%%%%%%%%%%%%
%
% Initial Conditions and Setup of Wave Equation FD Solution
%
%%%%%%%%%%%%%%%%%%%%%%%%%%%%%%%%%%%%%%%%%%%%%%%%%%%%%%%%%%%%%%%%%%%%%%%%%%%%
nmode=2; % mode
Xo=0.; % left boundary
Xe=ar; % right boundary
a=2*ar*st/(nmode*omega(1)); % wave speed
dt=.01/(2/nmode*st)/2; % time step
dx=(Xe-Xo)/(nz-1); % delta x value
X=Xo:dx:Xe; % spatial array
c=a*dt/dx; % Courant number (< 1 for stability)
Y=zeros(1,nz); % initialization of solution vectors
Yold=zeros(1,nz);
Ynew=zeros(1,nz);
nsteps=(2/nmode)*100*2;
damp=1/(1+b*dt/2);
t_end=1.; % end time value for iterations

%prescription of initial and boundary conditions

for i=1:nz
   %Y(i)=xko*(sin(nmode*pi.*X(i)/25));
   Y(i)=xko*randn(1);
   aoverd(i)=abs(Y(i))/xko*admax;       % phase lag calculation
   phase(i)=(slope2*aoverd(i)+xinter2)*2*pi/360;
   phase2(i)=phase(i); %+pi;
   phi(i)=(slope*aoverd(i)+xinter)*2*pi/360;
```

```
   phi2(i)=phi(i)+pi;
end

Y(1)=0;
Y(nz)=0;
%starter solution for leapfrog-scheme

t=0;
Yold=Y;
for i=2:nz-1
   Y(i)=Yold(i)+.5*c^2*(Yold(i-1)-2*Yold(i)+Yold(i+1));
end
t=t+dt;

%%%%%%%%%%%%%%%%%%%%%%%%%%%%%%%%%%%%%%%%%%%%%%%%%%%%%%%%%%%%%%%%%%%%%%%%%%%
%
% Start of Main Iteration Loop
%
%%%%%%%%%%%%%%%%%%%%%%%%%%%%%%%%%%%%%%%%%%%%%%%%%%%%%%%%%%%%%%%%%%%%%%%%%%%
count=0;

for n=1:ntime

   if (n+5) > ntime
    outa(:,n-(ntime-5))=mod(theta,1);
      outb(:,n-(ntime-5))=mod(theta2,1);
   end

   %%%%%%%%%%%%%%%%%%%%%%%%%%%%%%%%%%%%%%%%%%%%%%%%%%%%%%%%%%%%%%%%%%%%%%%%%%%
   %
   % Solution of Wave Equation
   %
   %%%%%%%%%%%%%%%%%%%%%%%%%%%%%%%%%%%%%%%%%%%%%%%%%%%%%%%%%%%%%%%%%%%%%%%%%%%

   for l=1:nsteps

      f=2*Cl/(pi*rho).*(sin(2*pi.*th-phase')-...
sin(2.*pi.*th2-phase2'));
      ftest(l+(n-1)*nsteps)=f(50)*pi*rho/2/Cl;
      for i=2:nz-1
       Ynew(i)=damp*(2*Y(i)-Yold(i)+c^2*(Y(i-1)-2*Y(i)+Y(i+1))+...
 b*dt/2*Yold(i)+f(i));
      end
```

```
   Ynew(1)=2*Y(1)-Yold(1)+c^2*(Y(nz-1)-2*Y(1)+Y(2));
   Ynew(nz)= 2*Y(nz)-Yold(nz)+c^2*(Y(nz-1)-2*Y(nz)+Y(2));
   Yold=Y;
      Y=Ynew;
      t=t+dt;
      yout(l+(n-1)*nsteps)=Y(25);
      if (n+5) > ntime
         y(:,(n-(ntime-5)-1)*nsteps+l)=Y';
      end
      for i=1:nz
       aoverd(i)=abs(Y(i))/xko*admax;       % phase lag calculation
    phase(i)=(slope2*aoverd(i)+xinter2)*2*pi/360;
         phase2(i)=phase(i);
         phi(i)=(slope*aoverd(i)+xinter)*2*pi/360;
         phi2(i)=phi(i)+pi;
      end
   th=(l-1)./nsteps.*(thetan-theta)+theta;
   th2=(l-1)./nsteps.*(thetan2-theta2)+theta2;

   end

   for k=1:nz;
      xkk(k)=k*ar/nz;
      thetan(k)=mod(thetan(k),1);
      thetan2(k)=mod(thetan2(k),1);
      theta(k)=thetan(k);
      theta2(k)=thetan2(k);
   end

   %%%%%%%%%%%%%%%%%%%%%%%%%%%%%%%%%%%%%%%%%%%%%%%%%%%%%%%%%%%%%%%%%%%%%%%%%%%%
   %
   % Start of Calculation of First and Second Shear Layers
   %
   %%%%%%%%%%%%%%%%%%%%%%%%%%%%%%%%%%%%%%%%%%%%%%%%%%%%%%%%%%%%%%%%%%%%%%%%%%%%

   for k=1:nz
        % right hand side circle map (F_n^k term)
Bmat(k)=theta(k)+omega(k)-...
Ko*Y(k)/(2*pi)*sin(2*pi*theta(k)-phi(k)-.5*pi);
       Bmat2(k)=theta2(k)+omega(k)-...
Ko*Y(k)/(2*pi)*sin(2*pi*theta2(k)-phi2(k)-.5*pi);
   end
```

```
   for k=1:nz
      temp(k)=Bmat(k);
      temp2(k)=Bmat2(k);
   end

   for k=2:nz-1
% right hand side diffusion coupling
       Bmat(k)=(1-2*eps(k))*temp(k)+...
eps(k-1)*temp(k-1)+eps(k+1)*temp(k+1);
       Bmat2(k)=(1-2*eps(k))*temp2(k)+...
eps(k-1)*temp2(k-1)+eps(k+1)*temp2(k+1);
   end

   % periodic boundary conditions
    Bmat(1)=(1-2*eps(1))*temp(1)+...
eps(nz-1)*temp(nz-1)+eps(2)*temp(2);
    Bmat(nz)=(1-2*eps(nz))*temp(nz)+...
eps(nz-1)*temp(nz-1)+eps(2)*temp(2);
    Bmat2(1)=(1-2*eps(1))*temp2(1)+...
eps(nz-1)*temp2(nz-1)+eps(2)*temp2(2);
    Bmat2(nz)=(1-2*eps(nz))*temp2(nz)+...
eps(nz-1)*temp2(nz-1)+eps(2)*temp2(2);
   % solve for theta at new time step
   thetan=inv(Amat)*Bmat';
   thetan2=inv(Amat)*Bmat2';

   if mod(n,200) == 0
      disp(n)
   end
   if n > 300
      slope2=-196; xinter2=50;
   end
end

out=[outa outb];

save wakepat2.dat out -ascii
save y_amp2.dat y -ascii
```